Single-dose immunisation with a multimerised SARS-CoV-2 receptor binding domain (RBD) induces an enhanced and protective response in mice

Ralf Salzer[1]*, Jordan J. Clark[2]*, Marina Vaysburd[1]*, Veronica T. Chang[1]*, Anna Albecka-Moreau[1], Leo Kiss[1], Parul Sharma[2], Andres Gonzalez Llamazares[1], Anja Kipar[2, 3], Julian A. Hiscox[2], Andrew Owen[4], A. Radu Aricescu[1], James P. Stewart[2], Leo C. James[1§], and Jan Löwe[1§]

1 - MRC Laboratory of Molecular Biology, Cambridge, UK

2 - Institute of Infection, Veterinary and Ecological Sciences, University of Liverpool, Liverpool, UK

3 – Laboratory for Animal Model Pathology, Institute of Veterinary Pathology, Vetsuisse Faculty, University of Zurich, Zurich, Switzerland

4 - Department of Pharmacology and Therapeutics, Centre of Excellence in Long-acting Therapeutics (CELT), University of Liverpool, UK.

* Contributed equally to this work

§ Corresponding authors: lcj@mrc-lmb.cam.ac.uk; jyl@mrc-lmb.cam.ac.uk

Keywords: COVID-19; SARS-CoV-2; coronavirus; vaccine candidate; subunit vaccine; RBD; Dps

ABSTRACT

The COVID-19 pandemic, caused by the SARS-CoV-2 coronavirus, has triggered a worldwide health emergency. So far, several different types of vaccines have shown strong efficacy. However, both the emergence of new SARS-CoV-2 variants and the need to vaccinate a large fraction of the world's population necessitate the development of alternative vaccines, especially those that are simple and easy to store, transport and administer. Here, we showed that ferritin-like Dps protein from hyperthermophilic *Sulfolobus islandicus* can be covalently coupled with different SARS-CoV-2 antigens via the SpyCatcher system, to form extremely stable and defined multivalent dodecameric vaccine nanoparticles that remain intact even after lyophilisation. Immunisation experiments in mice demonstrated that the SARS-CoV-2 receptor binding domain (RBD) coupled to Dps (RBD-S-Dps) shows particular promise as it elicited a higher antibody titre and an enhanced neutralising antibody response compared to the monomeric RBD. Furthermore, we showed that a single immunisation with the multivalent RBD-S-Dps completely protected hACE2-expressing mice from serious illness and led to efficient viral clearance from the lungs upon SARS-CoV-2 infection. Our data highlight that multimerised SARS-CoV-2 subunit vaccines are a highly efficacious modality, particularly when combined with an ultra-stable scaffold.

38 **INTRODUCTION**

39 On 11 March 2020 the World Health Organisation declared the COVID-19 outbreak, caused by
40 the SARS-CoV-2 virus, a pandemic (Cucinotta and Vanelli, 2020). Since then, COVID-19 and the
41 efforts to contain it have changed the lives of unprecedented numbers of people. For example,
42 in April 2020 3.9 billion people were affected by lockdown measures aimed to cut or at least
43 reduce the chain of transmission with widespread negative impacts on employment, education
44 and other health issues. According to the Johns Hopkins University there have so far been
45 151M confirmed COVID-19 cases globally (May 2021) and virtually every country has been
46 affected. Officially, 3.2M people have died from SARS-CoV-2 infection (2021a, 2021b).

47 SARS-CoV-2 belongs to the family of *Coronaviridae*, which contain a positive-stranded RNA
48 genome (Pal et al., 2020). The RNA is enveloped by a membrane that harbours four coat
49 proteins (Fig. 1A). On the inside of the virus, the nucleocapsid protein (NP) is crucial for RNA
50 packaging and viral release from host cells (Zeng et al., 2020). The Spike protein, which is
51 embedded in the virus' membranous envelope, is essential for the interaction with human
52 angiotensin-converting enzyme 2 (hACE2) (Ke et al., 2020). It is the interaction with hACE2 that
53 is thought to initiate the process that leads to cell entry of viral RNA and infection (Shang et
54 al., 2020). The Spike protein is translated as a single polypeptide that is proteolytically
55 processed into its two subunits, S1 and S2. The Spike of SARS-CoV-2 is a trimer consisting of
56 three S1-S2 heterodimers (Huang et al., 2020). For membrane fusion between the cell and the
57 virus to occur, two cleavage events within the Spike complex are required (Ke et al., 2020). A
58 protease cleavage site located between S1 and S2 is cleaved by the producer cell's proprotein
59 convertase furin during virus assembly (Papa et al., 2021) (Fig. 1A). The second cleavage site is
60 located in the S2 domain at position R797, and its hydrolysis by the target cell's surface
61 protease TMPRSS2 triggers membrane fusion and cell entry (Papa et al., 2021).

62 The SARS-CoV-2 receptor-binding domain (RBD) is located within the S1 subunit of the Spike.
63 It is the RBD that interacts directly with the host cell via the hACE2 receptor (Ke et al., 2020).
64 It is therefore not surprising that antibodies directed against the RBD or overlap with the ACE2
65 binding region are strongly neutralising, making the RBD a promising subunit vaccine candidate
66 (Ke et al., 2020; Seydoux et al., 2020). The RBD is glycosylated and contains four disulphide

67 bridges that contribute to its stability, necessitating its expression in mammalian cells, as is
68 also the case for the Spike.

69 To end the pandemic, vaccines are by far the most promising approach and vaccine
70 developments, clinical trials, approvals and mass roll-outs are in progress. So far, until May
71 2021, 89 COVID-19 vaccines have been tested in clinical trials. Of those, 36 are undergoing
72 safety trials, 27 are in the phase of large-scale testing, 6 vaccines are authorised for limited
73 use, and 8 vaccines are fully approved (2021a). All approved vaccines show good-to-excellent
74 protection against severe illness and preliminary data have shown that virus transmission is
75 significantly reduced in vaccinated individuals (Mahase, 2020; Thompson et al., 2021). Most of
76 the approved vaccines and those in late-stage trials are mRNA-based, vector-based,
77 inactivated viruses or DNA vaccines (Mahase, 2020). Vector- and RNA-based vaccines can often
78 be rapidly developed because they deliver the immunogen coding sequence rather than the
79 immunogen itself. Currently, only one vaccine candidate in late phase trials is a protein-based
80 subunit vaccine, Novavax (Mahase, 2021). Some subunit vaccines are amenable to processes
81 such as lyophilisation that remove the need for a complex storage and distribution cold-chain.
82 As such, they provide substantial advantages over nucleic-acid based vaccines in the quest for
83 complete and global vaccination. A second challenge facing global vaccination is the
84 emergence of viral variants, some of which are more infectious and/or cause more severe
85 illnesses, and reduce the efficacy of existing vaccines (Davies et al., 2021; Ferreira et al., 2021;
86 Kupferschmidt, 2021; Zhang et al., 2021). Repeat vaccinations directed against these variants,
87 but that use the same type of vaccine, could be problematic. This is because immunity is
88 generated against the vaccine vector itself, neutralising it before it can deliver its immunogen
89 cargo (Bottermann et al., 2018). It is anticipated that in future, several different types of
90 vaccines will be required to cope with emerging variants of SARS-CoV-2.

91 Previous work has shown that protein-based subunit vaccines directed against SARS-CoV-2
92 deliver high antibody responses in animal models (Tan et al., 2021; Wang et al., 2021).
93 Furthermore, subunit antigens have the potential to deliver a cheaper, boostable and more
94 robust alternative to nucleic-acid based vaccines (Dalvie et al., 2021; Gu et al., 2021; He et al.,
95 2021; Joyce et al., 2021; Kalathiya et al., 2021; Koenig et al., 2021; Ma et al., 2020; Powell et
96 al., 2021; Xiang et al., 2020). To explore the development of stable and efficient subunit vaccine
97 candidates, we covalently linked SARS-CoV-2 proteins expressed in mammalian and bacterial

98 cells with bacterially-expressed Dps from the hyperthermophilic archaeon *Sulfolubus*
99 *islandicus* (Gauss et al., 2006). Immunisation using SARS-CoV-2 RBD linked to Dps (RBD-S-Dps)
100 proved to be highly effective in eliciting an immune response and to produce neutralising
101 antibodies that inhibit cell entry *in vitro*. Furthermore, transgenic K18-hACE2 mice infected
102 with SARS-CoV-2 were completely protected from serious illness following a single
103 immunisation with RBD-S-Dps.

104 **RESULTS**

105 **Three multimerised SARS-CoV-2 antigen complexes**

106 We aimed to find a stable, convenient and non-bacterial display scaffold that would allow the
107 display and multimerisation of a range of SARS-CoV-2 antigens (Fig. 1A). Multimerisation has
108 been used for many years to increase the immunogenicity of different antigens through
109 multivalency, and this approach has also been recently shown to work well with SARS-CoV-2
110 antigens (Dalvie et al., 2021; Kalathiya et al., 2021; Powell et al., 2021; Wang et al., 2021).

111 For the purpose of stable multimerisation, we identified Dps (ORF SIL_0492) from *Sulfolobus*
112 *islandicus*. The source organism is an archaeon, which prefers pH ~3 and, as a
113 hyperthermophile, has adapted to grow optimally at temperatures of around 80 °C. The
114 intrinsic thermostability and environmental robustness of *S. islandicus* Dps make it an
115 outstanding candidate for the development of a multimerisation scaffold. Dps, a member of
116 the ferritin-like protein family, self-assembles into hollow, dodecameric spheres with 12
117 subunits, which are roughly 10 nm across (Gauss et al., 2006). Most ferritins assemble larger
118 spheres with 24 subunits. Also, in contrast to *bona fide* ferritin scaffolds, both the N- and the
119 C-termini of Dps are accessible on the outside of the sphere.

120 We aimed to test whether Dps could efficiently display Spike, RBD and also NP antigens of
121 SARS-CoV-2 (Fig. 1A). Spike and RBD cannot be expressed in folded form in *E. coli*, whereas NP
122 as well as Dps express and fold well in *E. coli*. Expression of soluble and multimeric antigens
123 genetically fused to Dps in mammalian cells (or *E. coli*) was unsuccessful, therefore we decided
124 to employ the SpyCatcher/SpyTag system to attach Dps to different antigens. The
125 SpyCatcher/SpyTag system forms isopeptide bonds between amino acid side chains of the
126 catcher domain and the peptidic tag (Brune and Howarth, 2018; Zakeri et al., 2012). ΔN1-
127 SpyCatcher002 (Khairil Anuar et al., 2019) was fused genetically to the N-terminus of Dps,
128 separated by an eight amino acid long GS linker and a hexa-histidine tag added for purification
129 purposes (SpyC2-Dps, Fig. 1B & C). We chose N-terminal linkage to Dps, SpyC2-Dps, rather than
130 Dps-SpyC2 since the coupling reactions were more efficient, but we did not explore this in any
131 detail. Both the N- and C- terminus of Dps are on the outside of the sphere and are accessible
132 for covalent coupling. For the antigens, SpyTag2 sequences were fused either at the N- or C-
133 termini, based on steric considerations (RBD-SpyT2, SpyT2-NP, Spike-SpyT2). Conjugation of

134 stabilised and trimeric Spike-SpyT2 to the dodecameric SpyC2-Dps leads to polymerisation due
135 to the multivalency of both partners. To overcome this problem, and to obtain a biochemically
136 defined sample, we co-transfected HEK 293T Lenti-X cells with two different plasmids in a 3 to
137 1 ratio, one expressing a SpyT2 version and one without SpyT2. This favoured the expression
138 of Spike trimers in which only one of the monomers contains the SpyTag. Stabilised, trimeric
139 and on average monovalent Spike-SpyT2 and also RBD-SpyT2 were purified from conditioned
140 media of HEK 293S GnT1$^{-/-}$ (for Spike-SpyT2) or Expi 293 (for RBD-SpyT2) cell cultures. SpyC2-
141 Dps and SpyT2-NP were purified from the cytosol of *E. coli* cells transformed with the
142 appropriate plasmids. All constructs possess histidine tags and were purified by immobilised
143 metal affinity chromatography (IMAC) and at least one additional size exclusion step (SEC).
144 Sequences of all proteins used can be found in Suppl. Table 1. Expression yields were excellent
145 in all cases: SpyC2-Dps yielded ~120 mg/L culture, RBD-SpyT2 ~40 mg/L culture, stabilised
146 trimeric and monovalent Spike-SpyT2 ~13 mg/L culture and SpyT2-NP ~60 mg/L culture of pure
147 proteins (Fig. 2A).

148 To achieve efficient coupling of scaffold and antigens, a molar excess of each of the three
149 purified antigens (RBD-SpyT2, SpyT2-NP, Spike-SpyT2) was mixed with SpyC2-Dps to facilitate
150 covalent coupling. Subsequent removal of excess antigens was accomplished by SEC using a
151 Superose 6 column (Fig. 2B). Coupling efficiency was analysed by SDS-PAGE, followed by
152 Coomassie staining (Fig. 2C). When the coupled samples were mixed with denaturating SDS
153 sample buffer without additional heating, we detected high molecular weight complexes that
154 we suggest represent dodecameric assemblies caused by Dps that survive SDS treatment ("RT"
155 lanes). Heating the samples to 99 °C led to the disappearing of the higher bands ("99" lanes),
156 confirming both the (SDS-) stability and the purity of the coupled and multimerised protein
157 samples. Note that there were no bands showing uncoupled SpyC2-Dps in any of the three Ag-
158 S-Dps samples, meaning that coupling used all 12 available Dps subunits.

159 Next, we analysed the integrity of the scaffold after the coupling reactions, as well as
160 homogeneity by electron microscopy (Fig. 2D). For the scaffold alone, SpyC2-Dps, we observed
161 the expected small and well-dispersed ~10 nm Dps spheres. Similar homogeneity and
162 monodispersity were observed for all three coupled Ag-S-Dps versions, RBD-S-Dps, NP-S-Dps
163 and Spike-S-Dps. The Ag-S-Dps complexes were larger than the scaffold alone as the Dps
164 spheres were densely surrounded by extra densities, indicating the success of the coupling and

165 the structural integrity of Ag-S-Dps complexes after the coupling reactions. We note that no
166 aggregation was observed for Spike-S-Dps, indicating that the co-transfection approach
167 produced mostly trimeric Spike proteins with only one SpyTag2 present. Taken together, we
168 showed that the scaffold and the three antigens could be produced easily and at high yields
169 and resulted in biochemically pure and defined Ag-S-Dps proteins that display 12 antigens on
170 each Dps scaffold.

171 To determine whether the coupled Ag-S-Dps complexes were stable in blood plasma for
172 immunisations, we mixed the RBD-S-Dps complex with human serum (clotted, not heat
173 inactivated, at a 1:3 volume ratio). The RBD-S-Dps complex was remarkably stable, with 50%
174 remaining intact after 37 h at 37 °C (Suppl. Fig. 1A & B). Given the stability of the Dps scaffold
175 both in serum and when exposed to denaturing conditions (SDS-PAGE, "RT" lane) (Fig. 2C), we
176 next investigated whether the coupled RBD-S-Dps sample would survive lyophilisation and
177 subsequent re-solubilisation. A lyophilised, dry sample would facilitate prolonged storage even
178 in the absence of refrigeration. We therefore freeze-dried RBD-S-Dps and after rehydration
179 found no evidence of precipitation or significantly reduced protein concentration by SDS-PAGE
180 (Suppl. Fig. 1C). There was also no disappearance of the SDS-stable high-molecular weight
181 band, indicating Dps sphere integrity was maintained after re-hydration. Finally, electron
182 microscopy analysis showed the rehydrated sample to be indistinguishable from the starting
183 material with no evidence of disintegration or aggregation (Suppl. Fig. 1D).

184 **Multimerisation by Dps greatly enhances immunogenicity, especially for RBD**

185 Having obtained the three multimerised antigen-Dps (Ag-S-Dps), we tested whether they
186 induce a stronger immune response than their monomeric equivalents. We immunised mice
187 with the following protocol: five male C57BL/6J mice per group were given 50 µg protein
188 subcutaneously on days zero and 23, and 25 µg on day 64 (using CpG 1668 as an adjuvant) (Fig.
189 3A). Blood samples were taken on days 13 (1st bleed), 34 (2nd bleed) and 74 (3rd bleed). After
190 the 1st boost on day 34, antigen-specific antibodies were detected in the sera from the mice
191 by ELISA (Fig. 3B). Substantially higher antibody titres were detected with multimerised Dps-
192 fused RBD and NP. Multimerisation only improved Spike titres modestly, which may be
193 expected given that Spike is already a trimer without Dps. After 74 days, and the second boost,
194 the specific antibody titres were further increased. Spike induced the weakest response and

195 multimerisation had the smallest effect. In contrast, RBD-S-Dps and NP-S-Dps induced
196 substantial increases in antibody titres compared to the non-multimerised versions. We also
197 analysed sera for antibodies against the scaffold protein itself (SpyC2-Dps). Sera from mice
198 immunised with coupled Ag-S-Dps complexes showed measurable but low antibody titres
199 against SpyC2-Dps. Anti-SpyC2-Dps responses remained low even after the second boost,
200 suggesting that the scaffold itself is poorly immunogenic and that in the context of the fusions
201 the antibody response is largely directed against the viral antigens displayed on the surface.
202 Taken together the data show that multimerised Ag-S-Dps complexes produce substantial
203 improvements in antibody titres over the uncoupled antigens. Overall, the strongest response
204 was observed for RBD-S-Dps.

205 Next, we tested the neutralisation activity of antibodies produced by the mice immunised with
206 RBD-S-Dps, RBD-SpyT2, Spike-S-Dps, and Spike-SpyT2. The mouse sera within each group were
207 pooled at day 34 (2nd bleed) or 74 (3rd bleed) and analysed using a pseudovirus infection assay
208 (note that NP-directed sera will not have an effect in this assay because pseudotyped viruses
209 do not contain NP). In this assay, a lentiviral vector expressing GFP is pseudotyped with Spike
210 protein from SARS-CoV-2 to obtain virions that display Spike in their envelope and infect cells
211 in an ACE2-dependent manner. As seen in Figure 3C, the day 34 sera pool of the multimerised
212 RBD-S-Dps group protected against pseudovirus infection up to a dilution of 1:400, whereas
213 the monomeric RBD-SpyT2 only showed a protective effect at a 1:100 dilution, and even then
214 only reduced infection by ~50%. Sera from mice immunised with multimeric Spike-S-Dps also
215 protected against infection, whilst Spike-SpyT2 sera were unable to neutralise at any of the
216 dilutions tested. The sera taken after 74 days had substantially increased neutralisation activity
217 (Fig. 3D). The sera from RBD-S-Dps-immunised mice gave the strongest protection: even at a
218 1:6400 dilution only ~10% infection could be detected. At this 1:6400 dilution, the monomeric
219 RBD-SpyT2 and Spike-S-Dps sera gave very little neutralisation. While pseudoviruses are widely
220 used to test the neutralisation activity of SARS-CoV-2 antisera, they are based on a lentiviral
221 rather than coronavirus particle and do not recapitulate live virus replication. We therefore
222 tested whether antibodies raised against multimeric RBD-S-Dps were capable of blocking a
223 spreading infection of a primary clinical isolate of SARS-CoV-2. Viral replication was measured
224 by RT-qPCR using probes against *NP* (gRNA) or *E* (sgRNA). RBD-S-Dps antisera from five
225 different animals all potently inhibited SARS-CoV-2 (Suppl. Fig. 2A & B). In contrast, the potency

226 of antisera raised against RBD-SpyT2 varied considerably between mice. We conclude that
227 immunisation with RBD-S-Dps not only produces the highest titre antibodies (Fig. 3B), but also
228 the most neutralising (Fig. 3C & D) and with reliable potency against live virus (Suppl. Fig. 2A &
229 B).

230 **Single-shot immunisation with multimerised RBD-S-Dps protects mice against SARS-CoV-2**
231 **infection**

232 Encouraged by these results, we wanted to know if antigen display on our Dps scaffold would
233 induce a sufficiently strong antibody response to protect animals from SARS-CoV-2 infection.
234 We selected our most potent immunogen, RBD-S-Dps, and used it to immunise mice transgenic
235 for human ACE2 (K18-hACE2) (Zheng et al., 2021). As a single dose vaccination regime offers
236 many downstream logistical and practical benefits, we opted to immunise only once and then
237 challenge with SARS-CoV-2 on day 28 (Fig. 4A). We immunised subcutaneously six K18-hACE2
238 mice with RBD-S-Dps, six with RBD-SpyT2 and six with PBS (always three female and three male
239 mice), each with 25 µg of the immunogens (except PBS control), plus CpG adjuvant. The anti-
240 Spike antibody response following immunisation was measured by ELISA on days 13 and 24
241 (before challenge) and on day 35, (seven days post-challenge). A strong anti-Spike antibody
242 titre was detected in RBD-S-Dps-immunised mice, but almost none for either RBD-SpyT2 or
243 PBS (Fig. 4D). Antibody titres remained high for RBD-S-Dps at days 24 and 35.

244 On day 28, animals were challenged with 10^4 PFU SARS-CoV-2. Mice in the PBS control and
245 RBD-SpyT2-immunised groups began to show clinical signs of illness and a decline in body
246 weight from day four post-infection (Fig. 4B), consistent with previous reports of infection in
247 naïve animals (Zheng et al., 2021). In contrast, mice immunised with multimerised RBD-S-Dps
248 maintained body weight until the day seven end point. There was a statistically significant
249 difference in weights between the RBD-S-Dps-immunised and PBS control groups from day
250 four, and between RBD-S-Dps- and RBD-SpyT2-immunised mice from day five (Fig. 4C). There
251 was no significant difference in weight loss between the RBD-SpyT2-immunised mice and PBS
252 controls at any time point, suggesting that, unlike RBD-S-Dps, non-multimerised RBD does not
253 provide protection after only a single vaccination. All animals were culled on day seven post-
254 infection and tissues collected for analysis. As mentioned, there were no significant changes in
255 anti-Spike antibody levels pre- versus post-challenge, indicating that mostly antibodies raised

256 during the immunisation contributed to the immune response during the infection (Fig. 4D).
257 SARS-CoV-2 infection of the lung was quantified by plaque assay and genomic and subgenomic
258 qPCR, using probes against the viral genes NP and E, respectively. There were significantly
259 lower levels of infectious virus in the lungs of mice immunised with RBD-S-Dps, compared to
260 either RBD-SpyT2 immunised or PBS control groups (Fig. 4E). A broadly similar pattern was
261 observed when quantifying virus by either genomic or subgenomic qPCR (Fig. 4F & G).
262 However, we noted a marked difference in the amounts detected between male *vs* female
263 mice. Female RBD-S-Dps-immunised mice had significantly fewer genomic and subgenomic
264 transcripts, compared to mice from other groups and their male equivalents (Fig. 4F & G and
265 Suppl. Fig. 3A & B). We attempted to correlate this with differences in antibody titres, but while
266 there was a trend towards lower titres in male mice, particularly just before and just after the
267 challenge, this was not significant (Suppl. Fig. 3C). A larger group size would be needed to
268 confirm this result. Despite these sex-dependent differences in the qPCR data, the near-
269 absence of infectious virus in both male and female RBD-S-Dps immunised mice, as measured
270 by plaque assay (Suppl. Fig. 3D), suggests they were both highly protected. Finally, we
271 examined the lungs of mice from the different groups for histopathological changes and for
272 viral antigen expression using an anti-NP antibody to reveal sites of replication (Fig. 4H, Suppl.
273 Fig. 4) and immune cell infiltration (Suppl. Fig. 5). A detailed description is provided in the
274 Supplementary Results. In summary, lungs from RBD-SpyT2-immunised mice or PBS control
275 mice showed substantial and wide-spread NP expression mainly in pneumocytes (Fig. 4H &
276 Suppl. Fig. 4), indicative of viral replication throughout the lobe and consistent with the high
277 virus levels measured in these animals (Fig. 4E-G). There was also evidence of pneumocyte
278 degeneration and syncytial cell formation, as has been reported in COVID-19 cases post-
279 mortem (Bussani et al., 2020). Multifocal leukocyte infiltration was observed, particularly in
280 PBS-control animals, dominated by macrophages, followed by T-cells (mainly CD4+ and lesser
281 CD8+ cells), B cells and neutrophils (Suppl. Fig. 4 & 5). This is reminiscent of the
282 hyperinflammation in post-mortem reports of lethal COVID-19 associated with
283 immunopathology (Schurink et al., 2020). In contrast, the lungs of mice protected by
284 multimerised RBD-S-Dps were either almost or entirely clear of NP expression (Suppl. Fig. 4)
285 and pathological changes (female mice), or showed only mild changes consistent with those
286 observed in the PBS-control animals (Suppl. Fig. 5), and markedly reduced NP expression.
287 Taken together, these data indicate that immunisation with RBD-S-Dps is highly protective

288 against SARS-CoV-2 in hACE2-expressing mice, even after a single dose, whilst monomeric RBD-
289 SpyT2 is not.

290 **DISCUSSION**

291 Here we have shown that the ferritin-like protein Dps from the hyperthermophile *S. islandicus*
292 possesses exceptional qualities as a SARS-CoV-2 subunit vaccine scaffold. We combined Dps
293 with the SpyCatcher/SpyTag system in order to create a "plug-and-play" system that allows
294 the rapid and facile synthesis of highly stable multimeric subunit vaccines. Mixing the
295 SpyCatcher-Dps protein with any compatible SpyTag antigen leads to the assembly of highly
296 monodisperse nanoparticles displaying exactly 12 antigens. Using this approach, we have
297 produced subunit vaccines based on Spike, RBD or NP from SARS-CoV-2 and tested them in
298 immunisation and viral challenge experiments. In each case, the Dps-displayed antigens out-
299 performed their non-multimerised equivalents and induced a more rapid and potent antibody
300 response.

301 Subunit vaccines offer distinct advantages in cost, simplicity, production capacity, storage,
302 transport and administration over nucleic-acid based vaccines (Pollet et al., 2021). Principle
303 amongst these considerations is stability, with currently used vaccines such as those produced
304 by Pfizer–BioNTech, Moderna and Oxford-AstraZeneca requiring a -80°C or -20°C cold-chain.
305 In countries without a highly developed logistical and medical infrastructure this represents a
306 significant impediment to vaccination. Whilst subunit vaccine development currently lags
307 behind nucleic-acid based equivalents, there is good evidence that such vaccines are
308 nevertheless effective at inducing a protective response. SARS-CoV-2 RBD by itself (Yang et al.,
309 2020) or in simple fusions such as to IgG Fc (Liu et al., 2020) have been shown to elicit SARS-
310 CoV-2-neutralising antibodies. Antigen multimerisation increases neutralising titres, for
311 instance when using ferritin as a scaffold (He et al., 2021; Powell et al., 2021). More complex
312 scaffolds have also been used, for instance virus-like icosahedral particles that display 60
313 antigen copies (e.g. I3-01) (Hsia et al., 2016). When fused directly to viral antigens (Walls et al.,
314 2020), or using the SpyCatcher/SpyTag system (Cohen et al., 2021; Tan et al., 2021) the I3-01
315 scaffold has been shown to induce a neutralising antibody response. Our scaffold differs from
316 those previously used to deliver SARS-CoV-2 immunogens in several important aspects. First,
317 because we have used a thermostable protein it is intrinsically more stable, providing potential
318 benefits to vaccine transport and storage and also to immunogen stability *in vivo*. Second, it is
319 smaller than other scaffolds (< 10 nm vs > 10 nm for ferritin or 25 nm for the I3-01
320 nanoparticle), making it an easier cargo for cellular uptake. Third, it displays fewer copies than

321 ferritin or I3-01 (12 vs 24 or 60, respectively), allowing the selection of higher-affinity B cells
322 and avoiding the activation of off-target (and possibly cross-reactive) B cell competitors (Kato
323 et al., 2020). Fourth, in contrast to *bona fide* ferritin scaffolds, the N- and the C-termini of Dps
324 are both accessible on the outside of the sphere. This allows, at east in principle, for the
325 conjugation of two discrete antigens onto a single scaffold, for example both SARS-CoV-2
326 Spike/RBD and NP to be displayed simultaneously.

327 Importantly, we have provided here data demonstrating the benefit of antigen
328 multimerisation in inducing not just neutralising antibodies but an immune response capable
329 of providing *in vivo* protection. In our SARS-CoV-2 challenge experiments, we found that RBD
330 alone failed to protect mice, which displayed continued weight-loss and high viral loads in the
331 lungs. In contrast, our Dps-based vaccine displaying RBD completely protected mice from
332 SARS-CoV-2-associated pneumonia and disease after only a single immunisation. We noted
333 however a difference in Dps-RBD induced protection between male and female mice, with the
334 latter having lower viral loads and hardly any pulmonary changes. Trial data for both mRNA
335 and vector-based vaccines has not been disaggregated by sex but data on SARS-CoV-2 infection
336 show that men are more at risk of severe adverse conditions, hospitalisation and death (Klein
337 et al., 2020; Scully et al., 2020). Our results support the consideration of sex as a variable in
338 vaccine trials (Bischof et al., 2020).

339 Further research is needed to develop the Dps-scaffold into a *bona fide* vaccine for SARS-CoV-
340 2 and other viruses. Replicating the robust neutralising antibody response and high-level of
341 protection achieved in mice from a single dose in humans will be crucial. Moreover, whilst
342 most studies of subunit vaccines have focused on antibodies, long-lasting protection is likely
343 to be dependent upon stimulating CD4+ and CD8+ T cell immunity (Sauer and Harris, 2020; Zuo
344 et al., 2021). Data from current vaccine trials and roll-outs has yet to be fully analysed but a
345 correctly balanced T cell response appears associated with recovery from acute infection and
346 the avoidance of hospitalisation and severe virus-induced immunopathology (Chen and John
347 Wherry, 2020). Fortunately, the analysis of T cell epitopes from SARS-CoV-2 convalescents
348 (Nelde et al., 2021) provides a basis for engineering subunit vaccines specifically to engage
349 both B and T cells. In this context, the ability of our Dps-scaffold to display antigens at both
350 termini may prove particularly beneficial. In addition to ensuring a well-balanced immune
351 response in humans, a more thorough investigation into the long-term stability, storage and

352 reconstitution of lyophilised material is required to demonstrate that a Dps-based vaccine is
353 suitable for use in regions with limited infrastructure. Future work notwithstanding, our data
354 add to a body of evidence that subunit-based vaccines represent a viable choice as a vaccine
355 modality for SARS-CoV-2. Whilst other vaccine formats are significantly more advanced,
356 subunit approaches such as Dps offer distinct advantages in simplicity of production, requiring
357 no proprietary technology, robustness of material and potency of protection.

358 **MATERIAL & METHODS**

359 **Cloning, expression and purification of the protein components**

360 **SpyC2-Dps:** a hexa-histidine tag was fused to ΔN1-SpyCatcher002, which was subsequently
361 linked to the Dps from *Sulfolobus islandicus* (ORF SIL_0492, GenBank AGJ61963.1), separated
362 by a GSEGSSGG-linker (Suppl. Table 1, SpyC2-Dps). The sequence was codon optimised for the
363 expression in *E. coli* and the gene was cloned into the pOPINS vector by Gibson assembly. The
364 plasmid encoding for SpyC2-Dps was transformed into C43(DE3) *E. coli*. Cells were grown at 37
365 °C in 2xYT medium to an OD_{600} of 0.8. Protein production was induced with 1 mM IPTG for 6 h.
366 Cells were harvested at 4500 x g for 25 min at room temperature (RT). Cells were shock-frozen
367 in liquid nitrogen (LN2) and stored at -80 °C. Cells producing SpyC2-Dps were re-suspended in
368 T-buffer1 (30 mM Tris, 250 mM NaCl, pH 8.0) with one tablet of Complete Protease Inhibitors
369 (Roche) per 10 g cells wet weight. Cell disruption was carried out using sonication for 7.5 min
370 "on" time, using a 50 % duty cycle. Cell debris were removed by centrifugation at 20,000 x g
371 for 30 min at RT. The supernatant was loaded onto a HisTrap FF affinity chromatography
372 column (Cytiva). Washing was carried out for 17 column volumes (CV) with T-buffer1 plus 110
373 mM imidazole. The protein was eluted with T-buffer1 containing 400 mM imidazole. Purity of
374 fractions was examined by SDS-PAGE and the purest fraction were pooled and concentrated
375 using a Vivaspin Turbo centrifugal concentrator (100,000 MWCO, Sartorius). Concentrated
376 sample was loaded onto a size-exclusion column (SEC, Sephacryl S-400, Cytiva), with PBS as
377 the running buffer. Purity was examined by SDS-PAGE and the sample was frozen in LN2 and
378 stored at -80 °C.

379 **SpyT2-NP:** the nucleocapsid protein (amino acids 48 - 364; GenBank: MN908947; NP) was
380 cloned into the vector pOP-TH and N-terminally equipped with a hexa-histidine tag (Pickering
381 et al., 2020). A SpyTag2 sequence separated by GS-rich linkers was inserted between the hexa-
382 histidine tag and NP (Fig. 1 & Suppl. Table 1, SpyT2-NP). The vector encoding for SpyT2-NP was
383 transformed into *E. coli* C41(DE3) cells. For protein expression, cells were grown at 37 °C in
384 2xYT medium to an OD_{600} of 0.7. Protein production was induced with 1 mM IPTG for 6 h. Cells
385 were harvested at 4500 x g for 25 min at 4 °C. Cells were frozen in LN2 and stored at -80 °C.
386 SpyT2-NP-producing cells were re-suspended in T-buffer2 (50 mM Tris, 1 M NaCl, 10 mM
387 imidazole, 2 mM DTT, pH 8.0) with Complete Protease Inhibitor added (1 tablet per 10 g cells

388 wet weight). Cells were lysed by sonication (3 mins total "on" time, duty cycle 50 %).
389 Precipitated proteins and cell debris were removed by centrifugation (40,000 x g, 1 h, 4 °C).
390 The supernatant was loaded onto a HisTrap FF affinity chromatography column and washed
391 with 20 CV T-Buffer3 (50 mM Tris, 300 mM NaCl, 1 mM DTT, pH 8.0) containing 20 mM
392 imidazole. Elution was carried out in T-buffer3 containing 400 mM imidazole. Elution fractions
393 containing NP were loaded onto 20 ml HiTrap Heparin HP column equilibrated in T-buffer4 (50
394 Tris, 1 mM DTT, pH 8.0). The column was washed with 3 CV T-buffer4. Elution was carried out
395 with a linear gradient of 0 - 2 M NaCl. Elution fractions containing SpyT2-NP were examined by
396 SDS-PAGE and pooled, and concentrated using a Vivaspin Turbo concentrator with a 10,000
397 MWCO (Sartorius). Concentrated sample was loaded onto a SEC column (Sephacryl S-200)
398 (Cytiva) in PBS + 250 mM additional NaCl. Purity was checked by SDS-PAGE and samples were
399 frozen in LN2 and stored at -80 °C.

400 **Spike-SpyT2 and Spike:** to express the ectodomain of the stabilised prefusion Spike protein
401 trimer (Wrapp et al., 2020) with only one subunit carrying the SpyTag2 tag, two constructs –
402 one with and one without a SpyTag2 - were made. First, a gene encoding residues 16-1208 of
403 SARS-CoV-2 Spike protein (GenBank: MN908947) with proline substitutions at residues 986
404 and 987, a GSAS substitution at the furin cleavage site (residue 682-685), a C-terminal T4
405 fibritin trimerisation motif, a GGSGGS linker, an HRV3C protease cleavage site, a GGS linker
406 and an AviTag, was synthesised and cloned into the lentiviral expression vector pHR-SFFV
407 (Chang et al., 2015, 2016; Elegheert et al., 2018) downstream of the sequence encoding the
408 chicken RPTPσ secretion signal peptide (cRPTPσSP) (Aricescu et al., 2006). Then, either a GGS
409 linker and a hexa-histidine tag, or a GGS linker, an octa-histidine tag, a GGSGGSGGS linker and
410 a SpyTag2 were inserted after the AviTag sequence to form two Spike constructs, with and
411 without a SpyTag2 (Suppl. Table 1, Spike-SpyT2 and Spike, respectively). For protein expression
412 and purification, please see the next paragraph.

413 **RBD-SpyT2**: a gene encoding residue 332-529 of SARS-CoV-2 Spike protein (constituting the
414 receptor binding domain, RBD) was synthesised and cloned downstream of cRPTPσ of the pHR-
415 SFFV vector and a GGSGGS linker, an AviTag, a GGS linker, an octa-histidine tag, a GGSGGSGGS
416 linker and a SpyTag2 were inserted at the 3' end of the gene (Suppl. Table 1, RBD-SpyT2). The
417 vectors for Spike-SpyT2, Spike and RBD-SpyT2 were used for protein production in the
418 mammalian lentiviral expression system (Chang et al., 2015, 2016; Elegheert et al., 2018). The

419 DNA of the constructs was mixed with the lentiviral envelope and packaging vectors pMD2-G
420 and psPAX2c (Addgene) and polyethylenimine (PEI, Sigma) to transiently transfect HEK 293T
421 Lenti-X cells (Takara/Clontech) to make lentiviral particles. To make Spike trimer protein with
422 only one subunit carrying a SpyTag2, the DNAs of constructs Spike and Spike-SpyT2 were used
423 at a molar ratio 3:1. The virus particles produced were used to infect HEK 293S GnT1-/- cells
424 (for Spike-SpyT2) or Expi 293 cells (for RBD-SpyT2). The infected cells were then expanded to
425 obtain 3 L cultures and conditioned media were harvested and sterile filtered (0.22 µm). The
426 supernatant was concentrated and the buffer exchanged to 25 mM Tris pH 8.0, 300 mM NaCl
427 using an Äkta flux tangential flow system (Cytiva). The conditioned supernatant was then
428 loaded onto a HisTrap column (Cytiva) and washed and eluted with 50 mM and 250 mM
429 imidazole in the same buffer, respectively. Eluted fractions were checked by SDS-PAGE, pooled
430 and further purified in PBS buffer by SEC on Superdex 200 for RBD and Superose 6 for trimeric
431 Spike protein (both Cytiva). Peak fractions were checked by SDS-PAGE again and frozen in LN2
432 and stored at -80 °C.

433 **Coupling and purification of multimerised complexes**

434 For the preparations of Ag-S-Dps complexes, comprising RBD-S-Dps, NP-S-Dps and Spike-S-Dps
435 the antigens: RBD-SpyT2, SpyT2-NP and Spike/Spike-SpyT2, and the scaffold protein SpyC2-
436 Dps were diluted in PBS buffer + 250 mM NaCl to 0.2 to 1 mg/mL and mixed. To achieve full
437 occupancy of SpyC2-Dps with the antigens, the molar ratio for SpyC2-Dps to RBD-SpyT2 was
438 1:1.3, for SpyT2-NP 1:2 and for trimeric Spike/Spike-SpyT2 1:2.5. Reactions were left for ~5 min
439 at RT and covalent coupling between SpyCather2 and SpyTag2 was checked by SDS-PAGE.
440 Subsequently, samples were concentrated using Vivaspin Turbo concentrators (100,000
441 MWCO). Antigen-decorated SpyC2-Dps complexes were separated from the excess antigens
442 by SEC in PBS + 250 mM NaCl on a Superose 6 Increase column (Cytiva). Fractions were checked
443 again for purity by SDS-PAGE, frozen in LN2 and stored at -80 °C.

444 **Negative-stain electron microscopy**

445 Proteins were diluted in PBS to concentrations of ~0.012 mg/mL. 3 µL of the solution were
446 applied to a glow-discharged carbon-coated grid and immediately blotted. For the staining, 10
447 µL of 2% (w/v) uranyl formate were applied and removed immediately by blotting the grid with

448 filter paper. Images were collected on a FEI Tecnai Spirit 120 kV electron microscope, equipped
449 with a CCD detector.

450 ***In vitro* human plasma stability assay**

451 The *in vitro* stability of RBD-S-Dps was studied in clotted human plasma (MD Biomedicals, cat.
452 #2930149). Stocks of the RBD-S-Dps samples (751.7 kDa per dodecameric complex) were
453 diluted in PBS to a final concentration of ~0.8 µM and subsequently mixed with pre-warmed
454 human plasma in a 1:3 (protein:plasma, v/v) ratio. The mixtures were incubated at 37 °C for
455 seven days. Samples were taken after 0, 1, 24, 48, 72, 96, 120 and 168 h, and immediately
456 mixed with denaturing gel-loading buffer, followed by 30 min incubation at 99 °C. Inactivated
457 samples were stored at -20 °C before the samples were diluted 1:10 with 1x SDS sample buffer
458 and 5 µL per sample were analysed by SDS-PAGE and Western blotting. The Ag-S-Dps
459 complexes were detected using the HisProbe-HRP (Thermo Fisher Scientific, TFS) and human
460 transferrin was used as a loading control and detected using transferrin antibodies from
461 chicken and chicken-HRP conjugated antibodies (Thermo Fisher Scientific, TFS, cat. #PA1-9525
462 and cat. # 31401).

463 **Lyophilisation of samples**

464 An aliquot of RBD-S-Dps of 120 µL (at a protein concentration of 1.4 mg/mL, in PBS buffer plus
465 additional 250 mM NaCl) was divided into a 40 µL control and a second aliquot of 80 µL. The
466 80 µL aliquot was lyophilised for 4 h at 30 °C with the aid of a vacuum concentrator (Eppendorf
467 Concentrator 5301) attached to a refrigerated condensation trap (Savant). After lyophilisation
468 to complete dryness, the sample was resuspended in 80 µL Milli-Q water. The sample was not
469 centrifuged or processed in any other way after rehydration. EM grids were prepared by
470 staining 1:20 and 1:100 dilutions (in PBS plus 250 mM NaCl) of lyophilised and resuspended
471 sample with 2 % uranyl formate solution on carbon-coated CF400-CU-UL grids (Electron
472 Microscopy Sciences) as described earlier. Imaging was also performed as described earlier. 10
473 µL of lyophilised and rehydrated sample and the untreated control were compared by SDS-
474 PAGE followed by Coomassie staining.

475 **Mouse immunisation (Fig. 3)**

476 Six weeks-old C57BL/6J mice (Jackson) were used in immunisation experiments, which were
477 conducted in accordance with the E7 moderate severity limit protocol and the UK Home Office
478 Animals (Scientific Procedures) Act (ASPA, 1986), and approved by the UKRI Animal Welfare
479 and Ethical Review Body. Mice were initially (prime) immunised subcutaneously with 50 µg of
480 the antigens in PBS, mixed with 10 µg CpG ODN 1668 adjuvant (InvivoGen). The following
481 antigens were used: RBD-S-DPS, RBD-SpyT2; NP-S-DPS, SpyT2-NP; Spike-S-DPS, Spike/Spike-
482 SpyT2 and SpyC2-Dps. Mice were subcutaneously boosted with 50 µg antigens at day 23 and
483 with 25 µg antigens at day 64. Tail bleeds for ELISA analyses were collected on days 13 and 34.

484 **Preparation of SARS-CoV-2 Spike-pseudotyped HIV-1 virions**

485 Replication deficient SARS-CoV-2 pseudotyped HIV-1 virions were prepared as described
486 previously (Morecroft and Thomas, 1988). Briefly, virions were produced in HEK 293T cells by
487 transfection with 1 µg of the plasmid encoding SARS CoV-2 Spike protein (pCAGGS-SpikeΔc19),
488 1 µg pCRV GagPol and 1.5 µg GFP-encoding plasmid (CSGW). Viral supernatants were filtered
489 through a 0.45 µm syringe filter at 48 h and 72 h post-transfection and pelleted for 2 h at
490 28,000 x g. Pelleted virions were drained and then resuspended in DMEM (Gibco).

491 **Spike-pseudotyped neutralisation assays with mouse sera**

492 HEK 293T-hACE2-TMPRSS2 cells were described previously (Papa et al., 2021). Cells were
493 plated into 96-well plates at a density of 0.75 x 10^3 cells per well and allowed to attach
494 overnight. 20 µL pseudovirus-containing supernatant was mixed with 2 µL dilutions of heat-
495 inactivated mouse sera and incubated for 40 min at RT. 10 µL of this mixture was added to
496 cells. 72 h later, cell entry was detected through the expression of GFP by visualisation on an
497 Incucyte S3 live cell imaging system (Sartorius). The percent of cell entry was quantified as GFP
498 positive areas of cells over the total area covered by cells. Entry inhibition by the sera was
499 calculated as percent virus infection relative to virus only control.

500 **ELISA assays**

501 96-well plates (Nunc) were coated overnight with 5 µg/mL of the indicated antigens. Plates
502 were blocked with MPBST: 2 % (v/v) milk in PBS, 0.05 % Tween 20. Polyclonal sera from
503 individual mice (challenge experiment) or mouse sera pooled within the same group (mouse

504 immunisation) were diluted as indicated with MPBST and incubated for 45 min on antigen-
505 coated plates. Plates were washed with MPBST and bound antibodies were detected with goat
506 anti-mouse IgG-HRP (Jackson Immunoresearch, #115-035-071).

507 **Cell culture and virus**

508 UK strain of SARS-CoV-2 (hCoV-2/human/Liverpool/REMRQ0001/2020; PANGO lineage B), was
509 used and grown to P4 in Vero E6 cells (Patterson et al., 2020). The intracellular viral genome
510 sequence and the titre of virus in the stock was determined by direct RNA sequencing
511 (Genbank: MW041156). The virus stock did not contain a deletion of the furin cleavage that
512 has been described previously during passage (Davidson et al., 2020).

513 **Mouse SARS-CoV-2 challenge experiment**

514 Animal work was approved by the local University of Liverpool Animal Welfare and Ethical
515 Review Body and performed under UK Home Office Project Licence PP4715265. Mice carrying
516 the human ACE2 gene under the control of the keratin 18 promoter (K18-hACE2; formally
517 B6.Cg-Tg(K18-ACE2)2Prlmn/J) were purchased from Jackson Laboratories. Mice were
518 maintained under SPF barrier conditions in individually ventilated cages. Animals were
519 randomly assigned into multiple cohorts and given 25 µg antigen (RBD-S-DPS or RBD-SpyT2) &
520 10 µg CpG or PBS via subcutaneous injection. On day 28 post-immunisation, mice were
521 anaesthetised lightly with isoflurane and inoculated intranasally with 50 µL containing 10^4 PFU
522 SARS-CoV-2 in PBS. They were culled on day 35 post-immunisation by an overdose of
523 pentabarbitone. Tissues were removed immediately for downstream processing.

524 **RNA extraction and DNase treatment**

525 The upper lobes of the right lung were dissected and homogenised in 1 mL of TRIzol reagent
526 (TFS) using a Bead Ruptor 24 (Omni International) at 2 meters per second for 30 s. The
527 homogenates were clarified by centrifugation at 12,000 x g for 5 min before full RNA extraction
528 was carried out according to manufacturer's instructions. RNA was quantified and quality
529 assessed using a Nanodrop (TFS) before a total of 1 µg was DNase treated using the TURBO
530 DNA-free kit (TFS) as per manufacturer's instructions.

531 **qRT-PCR for viral load**

532 Viral loads were quantified using the GoTaq® Probe 1-Step RT-qPCR System (Promega). For
533 quantification of SARS-COV-2 the nCOV_N1 primer/probe mix from the SARS-CoV-2 (2019-
534 nCoV) CDC qPCR Probe Assay (IDT) were utilised while the standard curve was generated via
535 10-fold serial dilution of the 2019-nCoV_N_Positive Control (IDT) from 10^6 to 0.1
536 copies/reaction. The E sgRNA primers and probe have been previously described (Wölfel et al.,
537 2020) and were utilised at 400 nM and 200 nM respectively. Murine 18S primers and probe
538 sequences were utilised at 400 nM and 200 nM respectively. The IAV primers and probe
539 sequences were published as part of the CDC IAV detection kit (20403211). The IAV reverse
540 genetics plasmid encoding the NS segment was diluted 10-fold from 10^6 to 0.1 copies/reaction
541 to serve as a standard curve. The thermal cycling conditions for all qRT-PCR reactions were as
542 follows: 1 cycle of 45 °C for 15 min and 1 cycle of 95 °C followed by 40 cycles of 95 °C for 15 s
543 and 60 °C for 1 min The 18S standard was generated by the amplification of a fragment of the
544 murine 18S cDNA using the primers F: ACCTGGTTGATCCTGCCAGGTAGC and R:
545 GCATGCCAGAGTCTCGTTCG. Similarly, the E sgRNA standard was generated by PCR using the
546 qPCR primers. cDNA was generated using the SuperScript IV reverse transcriptase kit (TFS) and
547 PCR carried out using Q5 High-Fidelity 2X Master Mix (New England Biolabs) as per
548 manufacturer's instructions. Both PCR products were purified using the QIAquick PCR
549 Purification Kit (Qiagen) and serially diluted 10-fold from 10^{10} to 10^4 copies/reaction to form
550 the standard curve.

551 **Histology and immunohistology**

552 The left lung lobes were fixed in formal saline for 24 h and routinely paraffin wax embedded.
553 Consecutive sections (3-5 µm) were either stained with haematoxylin and eosin (HE) or used
554 for immunohistology (IH). IH was performed to detect SARS-CoV-2 antigen and leukocyte
555 subtypes, i.e. T cells (CD3+, CD4+, CD8+), B cells (CD45R/B220+) and macrophages (Iba1+),
556 using the horseradish peroxidase (HRP) method and the following primary antibodies: rabbit
557 anti-SARS-CoV NP (Rockland, 200-402-A50), rabbit anti-mouse CD3 (clone SP7; Spring
558 Bioscience Corp.), rabbit anti-mouse CD4 (clone #1; SinoBiological), rabbit anti-mouse CD8
559 (D4W2Z; Cell Signaling Technology), rat anti-mouse CD45R (clone B220, BD Pharmingen),
560 rabbit anti-human Iba1/AIF1 (Wako, 019-19741). Briefly, after deparaffination, sections
561 underwent antigen retrieval in citrate buffer (pH 6.0; Agilent) (anti-SARS-CoV-2, -CD8, -CD45R,
562 -Iba1) or Tris-EDTA buffer, pH 9.0 (anti-CD3, -CD4) for 20 min at 98 °C and for 20 min at 37 °C

563 respectively, followed by incubation with the primary antibody overnight at 4 °C (anti-SARS-
564 CoV-2), 60 min at RT (anti-CD3, -CD8, -CD45R, -Iba1) or 60 min at 37 °C (anti-CD3, -CD4). This
565 was followed by blocking of endogenous peroxidase (peroxidase block, Agilent) for 10 min at
566 RT and incubation with the secondary antibody, EnVision+/HRP, Rabbit and Rat respectively
567 (Agilent) for 30 min at RT (anti-SARS-CoV, -CD8, -CD45R, -Iba1) or the Omni-Map anti Rb HRP
568 (Ventana) for 16 min at 37 °C (anti-CD3, -CD4), followed by EnVision FLEX DAB+ Chromogen in
569 Substrate buffer (Agilent; anti-SARS-CoV-2, -CD8, -CD45R, -Iba1) for 10 min at RT or the DAB-
570 Map-Kit (Ventana; anti-CD3, -CD4), all in an autostainer (Dako or Ventana). Sections were
571 subsequently counterstained with haematoxylin.

572 **REFERENCES**

573 Aricescu, A.R., Lu, W., and Jones, E.Y. (2006). A time- and cost-efficient system for high-level
574 protein production in mammalian cells. Acta Crystallogr D Biol Crystallogr *62*, 1243–1250.

575 Bischof, E., Wolfe, J., and Klein, S.L. (2020). Clinical trials for COVID-19 should include sex as a
576 variable. The Journal of Clinical Investigation *130*, 3350–3352.

577 Bottermann, M., Foss, S., van Tienen, L.M., Vaysburd, M., Cruickshank, J., O'Connell, K., Clark,
578 J., Mayes, K., Higginson, K., Hirst, J.C., et al. (2018). TRIM21 mediates antibody inhibition of
579 adenovirus-based gene delivery and vaccination. Proceedings of the National Academy of
580 Sciences of the United States of America *115*, 10440–10445.

581 Brune, K.D., and Howarth, M. (2018). New Routes and Opportunities for Modular Construction
582 of Particulate Vaccines: Stick, Click, and Glue. Frontiers in Immunology *9*, 1432.

583 Bussani, R., Schneider, E., Zentilin, L., Collesi, C., Ali, H., Braga, L., Volpe, M.C., Colliva, A.,
584 Zanconati, F., Berlot, G., et al. (2020). Persistence of viral RNA, pneumocyte syncytia and
585 thrombosis are hallmarks of advanced COVID-19 pathology. EBioMedicine *61*, 103104.

586 Chang, V.T., Spooner, R.A., Crispin, M., and Davis, S.J. (2015). Glycan Remodeling with
587 Processing Inhibitors and Lectin-Resistant Eukaryotic Cells. Methods in Molecular Biology
588 *1321*, 307–322.

589 Chang, V.T., Fernandes, R.A., Ganzinger, K.A., Lee, S.F., Siebold, C., McColl, J., Jonsson, P.,
590 Palayret, M., Harlos, K., Coles, C.H., et al. (2016). Initiation of T cell signaling by CD45
591 segregation at "close contacts." Nature Immunology *17*, 574–582.

592 Chen, Z., and John Wherry, E. (2020). T cell responses in patients with COVID-19. Nature
593 Reviews. Immunology *20*, 529–536.

594 Cohen, A.A., Gnanapragasam, P.N.P., Lee, Y.E., Hoffman, P.R., Ou, S., Kakutani, L.M., Keeffe,
595 J.R., Wu, H.J., Howarth, M., West, A.P., et al. (2021). Mosaic nanoparticles elicit cross-reactive
596 immune responses to zoonotic coronaviruses in mice. Science *371*, 735–741.

597 Cucinotta, D., and Vanelli, M. (2020). WHO Declares COVID-19 a Pandemic. Acta Bio-Medica :
598 Atenei Parmensis *91*, 157–160.

599 Dalvie, N.C., Rodriguez-Aponte, S.A., Hartwell, B.L., Tostanoski, L.H., Biedermann, A.M.,
600 Crowell, L.E., Kaur, K., Kumru, O., Carter, L., Yu, J., et al. (2021). Engineered SARS-CoV-2
601 receptor binding domain improves immunogenicity in mice and elicits protective immunity in
602 hamsters. BioRxiv 2021.03.03.433558.

603 Davidson, A.D., Williamson, M.K., Lewis, S., Shoemark, D., Carroll, M.W., Heesom, K.J., Zambon,
604 M., Ellis, J., Lewis, P.A., Hiscox, J.A., et al. (2020). Characterisation of the transcriptome and
605 proteome of SARS-CoV-2 reveals a cell passage induced in-frame deletion of the furin-like
606 cleavage site from the spike glycoprotein. Genome Medicine *12*, 68.

607 Davies, N.G., Abbott, S., Barnard, R.C., Jarvis, C.I., Kucharski, A.J., Munday, J.D., Pearson, C.A.B.,
608 Russell, T.W., Tully, D.C., Washburne, A.D., et al. (2021). Estimated transmissibility and impact
609 of SARS-CoV-2 lineage B.1.1.7 in England. Science *372*.

610 Elegheert, J., Behiels, E., Bishop, B., Scott, S., Woolley, R.E., Griffiths, S.C., Byrne, E.F.X., Chang,
611 V.T., Stuart, D.I., Jones, E.Y., et al. (2018). Lentiviral transduction of mammalian cells for fast,
612 scalable and high-level production of soluble and membrane proteins. Nature Protocols *13*,
613 2991–3017.

614 Ferreira, I., Datir, R., Papa, G., Kemp, S., Meng, B., Rakshit, P., Singh, S., Pandey, R., Ponnusamy,
615 K., Radhakrishnan, V.S., et al. (2021). SARS-CoV-2 B.1.617 emergence and sensitivity to vaccine-
616 elicited antibodies. BioRxiv 2021.05.08.443253.

617 Gauss, G.H., Benas, P., Wiedenheft, B., Young, M., Douglas, T., and Lawrence, C.M. (2006).
618 Structure of the DPS-like protein from Sulfolobus solfataricus reveals a bacterioferritin-like
619 dimetal binding site within a DPS-like dodecameric assembly. Biochemistry *45*, 10815–10827.

620 Gu, M., Torres, J.L., Greenhouse, J., Wallace, S., Chiang, C.-I., Jackson, A.M., Porto, M., Kar, S.,
621 Li, Y., Ward, A.B., et al. (2021). One dose of COVID-19 nanoparticle vaccine REVC-128 provides
622 protection against SARS-CoV-2 challenge at two weeks post immunization. BioRxiv
623 2021.04.02.438218.

624 He, L., Lin, X., Wang, Y., Abraham, C., Sou, C., Ngo, T., Zhang, Y., Wilson, I.A., and Zhu, J. (2021).
625 Single-component, self-assembling, protein nanoparticles presenting the receptor binding
626 domain and stabilized spike as SARS-CoV-2 vaccine candidates. Science Advances *7*.

627 Hsia, Y., Bale, J.B., Gonen, S., Shi, D., Sheffler, W., Fong, K.K., Nattermann, U., Xu, C., Huang,
628 P.S., Ravichandran, R., et al. (2016). Design of a hyperstable 60-subunit protein dodecahedron.
629 [corrected]. Nature *535*, 136–139.

630 Huang, Y., Yang, C., Xu, X.F., Xu, W., and Liu, S.W. (2020). Structural and functional properties
631 of SARS-CoV-2 spike protein: potential antivirus drug development for COVID-19. Acta
632 Pharmacologica Sinica *41*, 1141–1149.

633 Joyce, M.G., King, H.A.D., Naouar, I.E., Ahmed, A., Peachman, K.K., Cincotta, C.M., Subra, C.,
634 Chen, R.E., Thomas, P.V., Chen, W.H., et al. (2021). Efficacy of a Broadly Neutralizing SARS-CoV-
635 2 Ferritin Nanoparticle Vaccine in Nonhuman Primates. BioRxiv : The Preprint Server for
636 Biology.

637 Kalathiya, U., Padariya, M., Fahraeus, R., Chakraborti, S., and Hupp, T.R. (2021). Multivalent
638 Display of SARS-CoV-2 Spike (RBD Domain) of COVID-19 to Nanomaterial, Protein Ferritin
639 Nanocages. Biomolecules *11*.

640 Kato, Y., Abbott, R.K., Freeman, B.L., Haupt, S., Groschel, B., Silva, M., Menis, S., Irvine, D.J.,
641 Schief, W.R., and Crotty, S. (2020). Multifaceted Effects of Antigen Valency on B Cell Response
642 Composition and Differentiation In Vivo. Immunity *53*, 548-563 e8.

643 Ke, Z., Oton, J., Qu, K., Cortese, M., Zila, V., McKeane, L., Nakane, T., Zivanov, J., Neufeldt, C.J.,
644 Cerikan, B., et al. (2020). Structures and distributions of SARS-CoV-2 spike proteins on intact
645 virions. Nature *588*, 498–502.

646 Khairil Anuar, I.N.A., Banerjee, A., Keeble, A.H., Carella, A., Nikov, G.I., and Howarth, M. (2019).
647 Spy&Go purification of SpyTag-proteins using pseudo-SpyCatcher to access an oligomerization
648 toolbox. Nature Communications *10*, 1734.

649 Klein, S.L., Dhakal, S., Ursin, R.L., Deshpande, S., Sandberg, K., and Mauvais-Jarvis, F. (2020).
650 Biological sex impacts COVID-19 outcomes. PLoS Pathogens *16*, e1008570.

651 Koenig, P.A., Das, H., Liu, H., Kummerer, B.M., Gohr, F.N., Jenster, L.M., Schiffelers, L.D.J.,
652 Tesfamariam, Y.M., Uchima, M., Wuerth, J.D., et al. (2021). Structure-guided multivalent
653 nanobodies block SARS-CoV-2 infection and suppress mutational escape. Science *371*.

654 Kupferschmidt, K. (2021). New mutations raise specter of "immune escape." Science *371*, 329–
655 330.

656 Liu, Z., Xu, W., Xia, S., Gu, C., Wang, X., Wang, Q., Zhou, J., Wu, Y., Cai, X., Qu, D., et al. (2020).
657 RBD-Fc-based COVID-19 vaccine candidate induces highly potent SARS-CoV-2 neutralizing
658 antibody response. Signal Transduction and Targeted Therapy *5*, 282.

659 Ma, X., Zou, F., Yu, F., Li, R., Yuan, Y., Zhang, Y., Zhang, X., Deng, J., Chen, T., Song, Z., et al.
660 (2020). Nanoparticle Vaccines Based on the Receptor Binding Domain (RBD) and Heptad
661 Repeat (HR) of SARS-CoV-2 Elicit Robust Protective Immune Responses. Immunity *53*, 1315-
662 1330 e9.

663 Mahase, E. (2020). Covid-19: What do we know about the late stage vaccine candidates? Bmj
664 *371*, m4576.

665 Mahase, E. (2021). Covid-19: Novavax vaccine efficacy is 86% against UK variant and 60%
666 against South African variant. Bmj *372*, n296.

667 Morecroft, J.A., and Thomas, M.H. (1988). Radionuclide ejection fraction. The British Journal
668 of Surgery *75*, 188.

669 Nelde, A., Bilich, T., Heitmann, J.S., Maringer, Y., Salih, H.R., Roerden, M., Lubke, M., Bauer, J.,
670 Rieth, J., Wacker, M., et al. (2021). SARS-CoV-2-derived peptides define heterologous and
671 COVID-19-induced T cell recognition. Nature Immunology *22*, 74–85.

672 Pal, M., Berhanu, G., Desalegn, C., and Kandi, V. (2020). Severe Acute Respiratory Syndrome
673 Coronavirus-2 (SARS-CoV-2): An Update. Cureus *12*, e7423.

674 Papa, G., Mallery, D.L., Albecka, A., Welch, L.G., Cattin-Ortola, J., Luptak, J., Paul, D., McMahon,
675 H.T., Goodfellow, I.G., Carter, A., et al. (2021). Furin cleavage of SARS-CoV-2 Spike promotes
676 but is not essential for infection and cell-cell fusion. PLoS Pathogens *17*, e1009246.

677 Patterson, E.I., Prince, T., Anderson, E.R., Casas-Sanchez, A., Smith, S.L., Cansado-Utrilla, C.,
678 Solomon, T., Griffiths, M.J., Acosta-Serrano, A., Turtle, L., et al. (2020). Methods of Inactivation

679 of SARS-CoV-2 for Downstream Biological Assays. The Journal of Infectious Diseases *222*, 1462–
680 1467.

681 Pickering, S., Betancor, G., Galao, R.P., Merrick, B., Signell, A.W., Wilson, H.D., Kia Ik, M.T.,
682 Seow, J., Graham, C., Acors, S., et al. (2020). Comparative assessment of multiple COVID-19
683 serological technologies supports continued evaluation of point-of-care lateral flow assays in
684 hospital and community healthcare settings. PLoS Pathogens *16*, e1008817.

685 Pollet, J., Chen, W.H., and Strych, U. (2021). Recombinant protein vaccines, a proven approach
686 against coronavirus pandemics. Advanced Drug Delivery Reviews *170*, 71–82.

687 Powell, A.E., Zhang, K., Sanyal, M., Tang, S., Weidenbacher, P.A., Li, S., Pham, T.D., Pak, J.E.,
688 Chiu, W., and Kim, P.S. (2021). A Single Immunization with Spike-Functionalized Ferritin
689 Vaccines Elicits Neutralizing Antibody Responses against SARS-CoV-2 in Mice. ACS Central
690 Science *7*, 183–199.

691 Sauer, K., and Harris, T. (2020). An Effective COVID-19 Vaccine Needs to Engage T Cells.
692 Frontiers in Immunology *11*, 581807.

693 Schurink, B., Roos, E., Radonic, T., Barbe, E., Bouman, C.S.C., de Boer, H.H., de Bree, G.J., Bulle,
694 E.B., Aronica, E.M., Florquin, S., et al. (2020). Viral presence and immunopathology in patients
695 with lethal COVID-19: a prospective autopsy cohort study. The Lancet. Microbe *1*, e290–e299.

696 Scully, E.P., Haverfield, J., Ursin, R.L., Tannenbaum, C., and Klein, S.L. (2020). Considering how
697 biological sex impacts immune responses and COVID-19 outcomes. Nature Reviews.
698 Immunology *20*, 442–447.

699 Seydoux, E., Homad, L.J., MacCamy, A.J., Parks, K.R., Hurlburt, N.K., Jennewein, M.F., Akins,
700 N.R., Stuart, A.B., Wan, Y.H., Feng, J., et al. (2020). Characterization of neutralizing antibodies
701 from a SARS-CoV-2 infected individual. BioRxiv : The Preprint Server for Biology.

702 Shang, J., Wan, Y., Luo, C., Ye, G., Geng, Q., Auerbach, A., and Li, F. (2020). Cell entry
703 mechanisms of SARS-CoV-2. Proceedings of the National Academy of Sciences of the United
704 States of America *117*, 11727–11734.

705 Tan, T.K., Rijal, P., Rahikainen, R., Keeble, A.H., Schimanski, L., Hussain, S., Harvey, R., Hayes,
706 J.W.P., Edwards, J.C., McLean, R.K., et al. (2021). A COVID-19 vaccine candidate using
707 SpyCatcher multimerization of the SARS-CoV-2 spike protein receptor-binding domain induces
708 potent neutralising antibody responses. Nature Communications *12*, 542.

709 Thompson, M.G., Burgess, J.L., Naleway, A.L., Tyner, H.L., Yoon, S.K., Meece, J., Olsho, L.E.W.,
710 Caban-Martinez, A.J., Fowlkes, A., Lutrick, K., et al. (2021). Interim Estimates of Vaccine
711 Effectiveness of BNT162b2 and mRNA-1273 COVID-19 Vaccines in Preventing SARS-CoV-2
712 Infection Among Health Care Personnel, First Responders, and Other Essential and Frontline
713 Workers - Eight U.S. Locations, December 2020-March 2021. MMWR. Morbidity and Mortality
714 Weekly Report *70*, 495–500.

715 Walls, A.C., Fiala, B., Schafer, A., Wrenn, S., Pham, M.N., Murphy, M., Tse, L.V., Shehata, L.,
716 O'Connor, M.A., Chen, C., et al. (2020). Elicitation of Potent Neutralizing Antibody Responses
717 by Designed Protein Nanoparticle Vaccines for SARS-CoV-2. Cell *183*, 1367-1382 e17.

718 Wang, W., Huang, B., Zhu, Y., Tan, W., and Zhu, M. (2021). Ferritin nanoparticle-based SARS-
719 CoV-2 RBD vaccine induces a persistent antibody response and long-term memory in mice.
720 Cellular & Molecular Immunology *18*, 749–751.

721 Wölfel, R., Corman, V.M., Guggemos, W., Seilmaier, M., Zange, S., Müller, M.A., Niemeyer, D.,
722 Jones, T.C., Vollmar, P., Rothe, C., et al. (2020). Virological assessment of hospitalized patients
723 with COVID-2019. Nature *581*, 465–469.

724 Wrapp, D., Wang, N., Corbett, K.S., Goldsmith, J.A., Hsieh, C.L., Abiona, O., Graham, B.S., and
725 McLellan, J.S. (2020). Cryo-EM structure of the 2019-nCoV spike in the prefusion conformation.
726 Science *367*, 1260–1263.

727 Xiang, Y., Nambulli, S., Xiao, Z., Liu, H., Sang, Z., Duprex, W.P., Schneidman-Duhovny, D., Zhang,
728 C., and Shi, Y. (2020). Versatile and multivalent nanobodies efficiently neutralize SARS-CoV-2.
729 Science *370*, 1479–1484.

730 Yang, J., Wang, W., Chen, Z., Lu, S., Yang, F., Bi, Z., Bao, L., Mo, F., Li, X., Huang, Y., et al. (2020).
731 A vaccine targeting the RBD of the S protein of SARS-CoV-2 induces protective immunity.
732 Nature *586*, 572–577.

733 Zakeri, B., Fierer, J.O., Celik, E., Chittock, E.C., Schwarz-Linek, U., Moy, V.T., and Howarth, M.
734 (2012). Peptide tag forming a rapid covalent bond to a protein, through engineering a bacterial
735 adhesin. Proceedings of the National Academy of Sciences of the United States of America *109*,
736 E690-7.

737 Zeng, W., Liu, G., Ma, H., Zhao, D., Yang, Y., Liu, M., Mohammed, A., Zhao, C., Yang, Y., Xie, J.,
738 et al. (2020). Biochemical characterization of SARS-CoV-2 nucleocapsid protein. Biochemical
739 and Biophysical Research Communications *527*, 618–623.

740 Zhang, W., Davis, B.D., Chen, S.S., Sincuir Martinez, J.M., Plummer, J.T., and Vail, E. (2021).
741 Emergence of a Novel SARS-CoV-2 Variant in Southern California. Jama *325*, 1324–1326.

742 Zheng, J., Wong, L.R., Li, K., Verma, A.K., Ortiz, M.E., Wohlford-Lenane, C., Leidinger, M.R.,
743 Knudson, C.M., Meyerholz, D.K., McCray, P.B., Jr., et al. (2021). COVID-19 treatments and
744 pathogenesis including anosmia in K18-hACE2 mice. Nature *589*, 603–607.

745 Zuo, J., Dowell, A.C., Pearce, H., Verma, K., Long, H.M., Begum, J., Aiano, F., Amin-Chowdhury,
746 Z., Hallis, B., Stapley, L., et al. (2021). Robust SARS-CoV-2-specific T cell immunity is maintained
747 at 6 months following primary infection. Nature Immunology.

748 (2021a). The New York Times, Coronavirus Vaccine Tracker (The New York Times).

749 (2021b). World Health Organization, COVID-19 situation reports.

750

751 **ACKNOWELDGEMENTS**

752 We thank Mark Wing and Kevin O'Connell (MRC-LMB, Cambridge). We would especially like to
753 thank the biomedical research staff at Liverpool and the LMB's Ares facility for their help and
754 support, as well as the technical staff of the Histology Laboratory, Institute of Veterinary
755 Pathology, Vetsuisse Faculty Zurich. Work at the MRC-LMB was funded by the Medical
756 Research Council, UK (U105184326 to JL, U105181010 to LCJ, MC_UP_1201/15 and
757 MR/L009609/1 to ARA) and Wellcome, UK (203276/C/16/Z to JL, 200594/Z/16/Z and
758 214344/A/18/Z to LCJ). Work in Liverpool was funded in by the Medical Research Council, UK
759 (MR/W005611/1 to JPS and JAH) and the US Food and Drug Administration, USA
760 (75F40120C00085 to JAH).

761

762 **CONFLICTS OF INTEREST**

763 The authors declare no competing interests.

764 **FIGURE LEGENDS**

765 **Figure 1. Overview of the multimerisation strategy employed and the antigens and scaffold**
766 **used. A**) Cartoon representation of SARS-CoV-2 binding to a human cell membrane. **B**)
767 Schematic diagram of the *Sulfolobus islandicus* Dps and SpyCatcher2-based display and
768 multimerisation strategy employed in this study. **C**) Diagram of the proteins used in this work.
769 SpyC2 is the SpyCatcher2 domain and SpyT2 is the peptidic SpyTag2 that becomes covalently
770 linked to SpyC2 upon simple mixing. Stabilised, trimeric Spike/Spike-SpyT2 contained on
771 average only one SpyT2 tag in order to avoid uncontrolled oligomerisation when coupled to
772 Dps.

773 **Figure 2: Preparation and quality control of coupled antigen – Dps complexes (Ag-S-Dps). A**)
774 SDS-PAGE of the three expressed and purified antigens as introduced in Fig. 1C. Glycosylation
775 of Spike leads to a fuzzy appearance of its band. RBD-SpyT2 and Spike-SpyT2 were expressed
776 in mammalian cells, SpyT2-NP was expressed in bacteria, as was the SpyC2-Dps scaffold. **B**)
777 Size-exclusion chromatography to separate excess antigens after the SpyCatcher2/Spytag2
778 coupling reactions; Superose 6 Increase in PBS. **C**) SDS-PAGE of the coupled and purified Ag-S-
779 Dps complexes. "RT", no heating; "99", heated to 99°C. The SpyC2-Dps scaffold alone, as well
780 as all the three coupled complexes show high-molecular weight complexes, presumably
781 dodecameric, that disappear only after heating of the samples in SDS loading buffer. **D**)
782 Negative-stain electron microscopy analyses of the three multimeric Ag-S-Dps complexes,
783 showing that all samples form defined and monodisperse spheres that display the antigens on
784 their surface, leading to particles of different sizes for the three differently-sized antigens.

785 **Figure 3: Mouse immunisation – multimeric Ag-S-Dps complexes elicit a powerful and**
786 **neutralising antibody response in mice. A**) Immunisation protocol. **B**) Bleeds on day 34 and 74
787 were tested for binding activity by ELISA against Spike-SpyT2, NP-SpyT2 or polymeric scaffold,
788 SpyC2-Dps. In all cases did the multimerised Ag-S-Dps complexes produce more antibodies
789 than the non-multimerised versions. RBD-S-Dps and NP-S-Dps produced very strong
790 responses. **C**) Pseudoviral cell entry neutralisation assay with sera from the 2nd bleed. Sera from
791 immunised mice were tested for neutralisation activity against a Spike-pseudotyped lentiviral
792 GFP vector (hence NP-S-Dps sera will not neutralise). Relative infection is plotted 72 hrs after
793 vector addition by quantifying GFP expression in HEK 293T ACE2/TMPRSS2 target cells. The

794 multimerised RBD-S-Dps and Spike-S-Dps showed strong neutralisation, in contrast to their
795 non-multimerised precursors. **D**) Same as C) but using sera from the 3rd bleed. Neutralisation
796 activity is enhanced in all sera, and the differential between multimerised and non-
797 multimerised antigens remains. Overall, RBD-S-Dps showed the strongest neutralisation
798 activity.

799 **Figure 4: Single-shot immunisation and Sars-CoV-2 challenge experiment using hACE2-mice.**
800 **A)** Immunisation and challenge protocol. **B**) K18-hACE2 mice were immunised with 25 µg of
801 RBD-S-Dps, RBD-SpyT2 or given PBS, plus 10 µg CpG adjuvant. The animals were challenged on
802 day 28 with 10^4 PFU SARS-CoV-2 and changes in weight recorded. The animals in the PBS
803 control group and those who had been given RBD-SpyT2 showed the characteristic weight loss
804 after four days post infection. RBD-S-Dps-immunised mice showed no such weight loss. **C**) Two-
805 way ANOVA tests on the weight changes between groups, as plotted in B). **D**) Sera from days
806 13, 24 and 35 were tested for anti-RBD antibodies by ELISA. Only RBD-S-Dps mice showed
807 significant antibody. **E**) Plaque assay using lung homogenates from mice culled seven days
808 post-infection. RBD-S-Dps-immunised mice contained very low amounts of infectious SARS-
809 CoV-2 in their lungs. **F) and G**) Genomic and subgenomic (gRNA, sgRNA) qPCR on RNA extracted
810 from lung homogenates, using probes against NP or E, respectively. Two-way ANOVA tests
811 were carried out with significance levels of: p = < 0.05 (*), p = < 0.05 (**), p = < 0.005 (***), p
812 = < 0.0005 (****). **H)** Representative lung sections from animals (n=6) taken seven days post-
813 challenge, stained by immunohistology for SARS-CoV-2 NP protein.

814 **FIGURES**

815 **Figure 1**

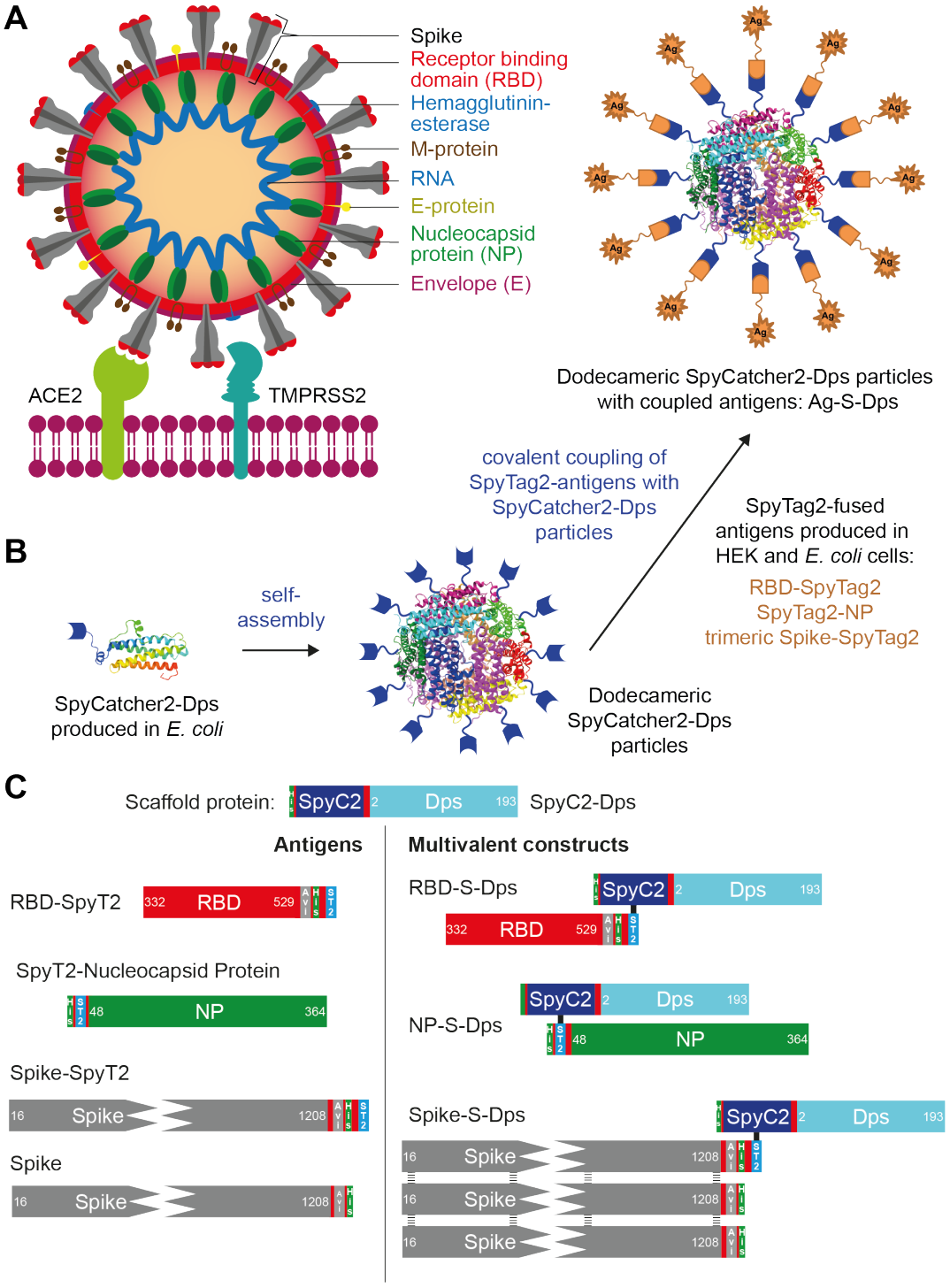

816

817

818 **Figure 2**

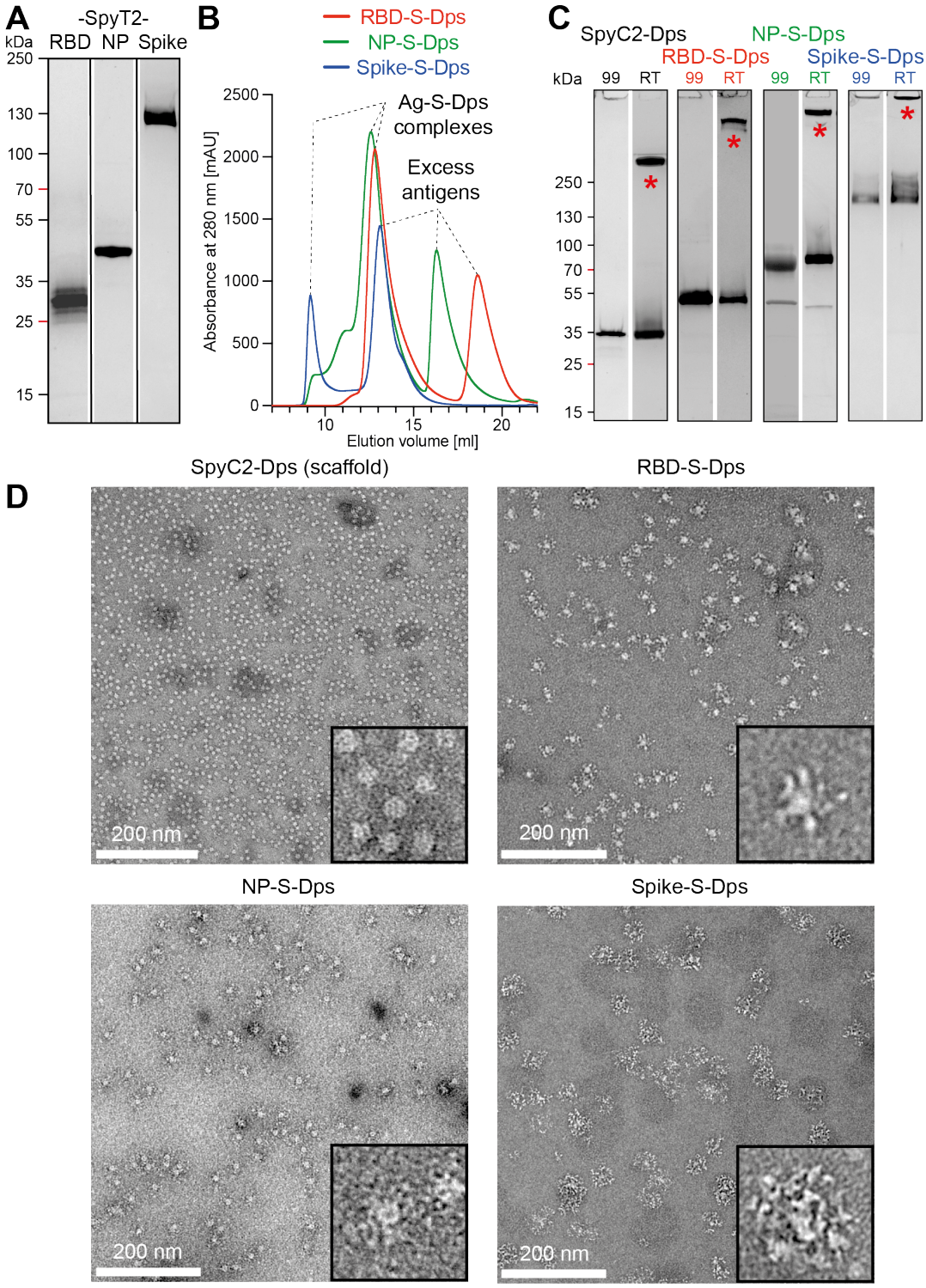

819

820 **Figure 3**

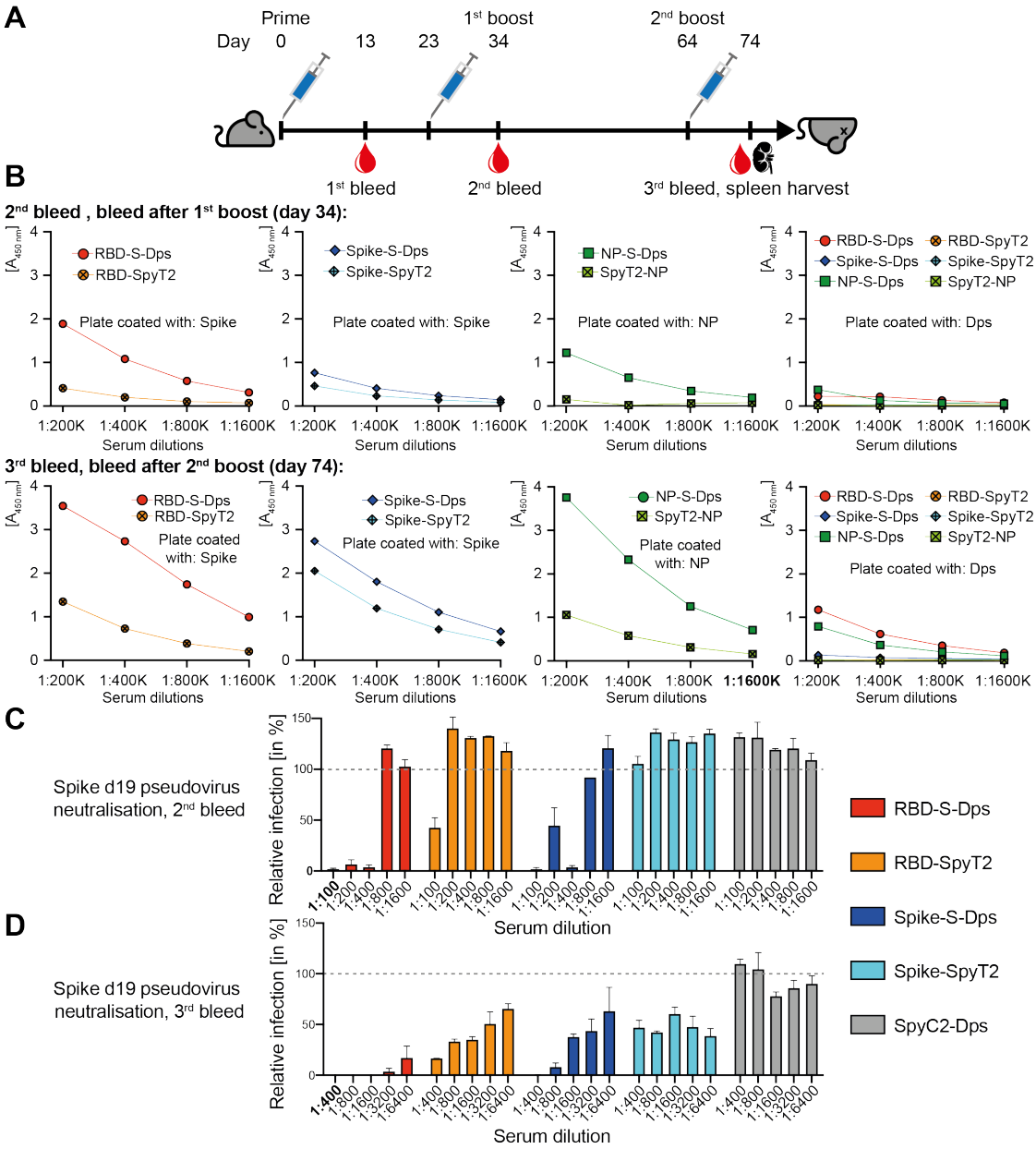

821

822

Figure 4

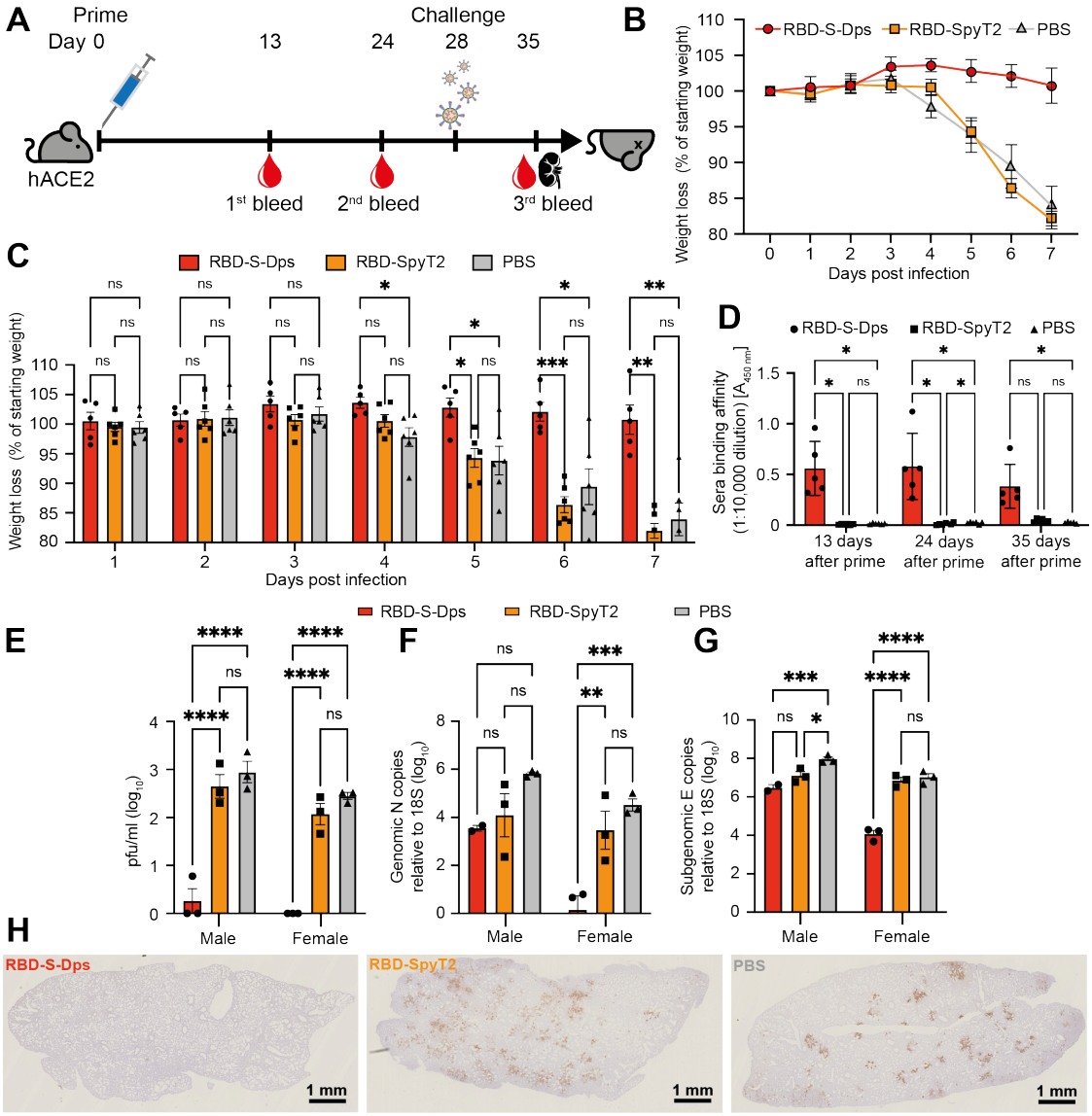
A
Prime
Day 0
13
24
Challenge
28
35
hACE2
1st bleed
2nd bleed
3rd bleed
B
RBD-S-Dps
RBD-SpyT2
PBS
Weight loss (% of starting weight)
Days post infection
C
RBD-S-Dps
RBD-SpyT2
PBS
Weight loss (% of starting weight)
Days post infection
D
RBD-S-Dps
RBD-SpyT2
PBS
Sera binding affinity (1:10,000 dilution) [A450 nm]
13 days after prime
24 days after prime
35 days after prime
E
pfu/ml (log10)
Male
Female
F
Genomic N copies relative to 18S (log10)
Male
Female
G
Subgenomic E copies relative to 18S (log10)
Male
Female
H
RBD-S-Dps
RBD-SpyT2
PBS
1 mm

825 **SUPPLEMENTAL INFORMATION**

826 **SUPPLEMENTAL RESULTS**

827 Detailed description of the lung histology in RBS-D-Dps-immunised mice subsequently
828 challenged with SARS-Cov-2 (Fig. 4A):

829 **Mice immunised with PBS control.** All animals showed a mild to moderate increase in
830 interstitial cellularity and multifocal extensive areas of consolidation due to macrophage and
831 lymphocyte infiltration, with a few neutrophils and with abundant activated type II cells,
832 occasional syncytial cells and some degenerate cells and moderate mesothelial cell activation
833 above the affected parenchymal area (Suppl. Fig. 4A). The changes were associated with
834 extensive viral antigen expression in type I and type II pneumocytes both in consolidated areas
835 and in alveoli without inflammatory changes. Occasional macrophages in the infiltrate also
836 appeared to express viral antigen (Suppl. Fig. 4B). Macrophages (Iba1+) were the dominant
837 cells in the infiltrates (Suppl. Fig. 5A), followed by numerous T cells with a relatively high
838 proportion and CD4 positive cells and less CD8 positive cells (Suppl. Fig. 5C, E, G), and a
839 moderate number of B cells (Suppl. Fig. 5I). There were also areas where alveoli exhibited type
840 II cell activation and desquamation, with desquamation of alveolar macrophages and some
841 neutrophils in the lumen. In addition, mild to moderate mononuclear vasculitis (mainly
842 arteritis) was seen (Suppl. Fig. 4A). Also, the infiltrate was dominated by macrophages,
843 followed by T cells (CD4 positive cells and less CD8 positive cells) and fewer B cells.

844 **Mice immunised with monomeric RBD-SpyT2.** All animals showed a mild to moderate
845 increase in interstitial cellularity and multifocal extensive areas of consolidation similar in
846 composition and extent to those seen in the PBS-control mice (Suppl. Fig. 4C). Viral antigen
847 was detected in multiple variably-sized foci, in type I and II pneumocytes and in macrophages
848 within and close to consolidated areas (Suppl. Fig. 4D).

849 **Mice immunised with multimerised RBD-S-Dps**. The three female animals showed minimal
850 histological changes in the lungs (Suppl. Fig. 4E). Besides a very mild increase in interstitial
851 cellularity, with rare T cells (both CD4 and CD8 positive cells) and B cells, one animal showed
852 scattered small focal leukocyte aggregates. Viral antigen expression was restricted to a few
853 macrophages in the leukocyte aggregates in the latter animal, while a second had positive

854 pneumocyte in an alveolus; in the third lung, viral antigen was not detected (Suppl. Fig. 4F). In
855 male animals, multifocal inflammatory infiltrates with viral antigen expression and mild
856 vasculitis similar to the other two groups, but substantially less extensive were seen (Suppl.
857 Fig. 4G, H). Also here, macrophages were the dominant cells in the focal infiltrates (Suppl. Fig.
858 5B), followed by the T cells (Suppl. Fig. 5D). The T cell population showed a mild shift in
859 composition, as now CD8-positive cells were as numerous or more frequent than CD4-positive
860 cells (Suppl. Fig. 5F-H). CD8-positive cells were also seen within alveolar lumina (Suppl. Fig. 5B
861 inset). B cells were found in moderate numbers in the infiltrates, in one animal they also
862 formed peribronchiolar aggregates (Suppl. Fig. 5J).

863

SUPPLEMENTAL FIGURES & TABLES

Supplemental Figure 1

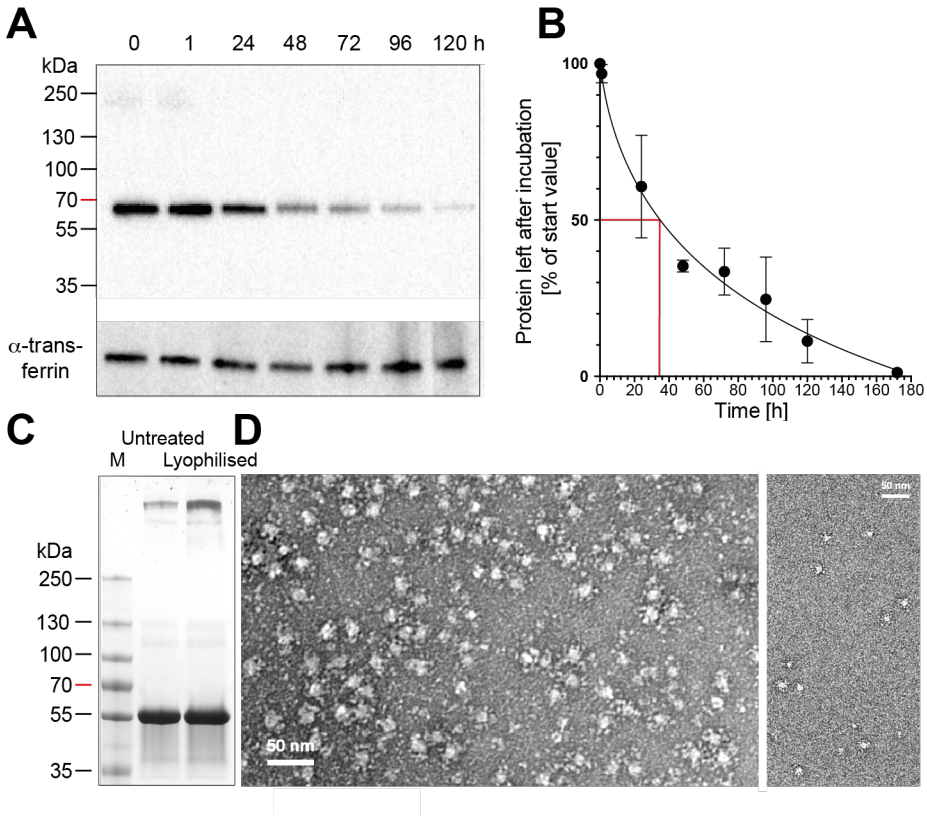

A) Plasma stability assay. RBD-S-Dps was incubated with non-heated human blood plasma for the amount of time indicated. SDS-PAGE and Western blot against the histidine tag on the protein. Transferrin was used as loading control and also detected by Western blot. **B)** Quantification of the data in A). The red line indicates the half-life of RBD-S-Dps under the conditions used. **C)** SDS-PAGE of RBD-S-Dps before and after lyophilisation. (Coomassie staining). **(D)** The lyophilised sample from C) was diluted to two different concentrations to demonstrate monodispersity and subjected to negative stain electron microscopy (left 20 x dilution and right 100 x dilution).

876 **Supplemental Figure 2**

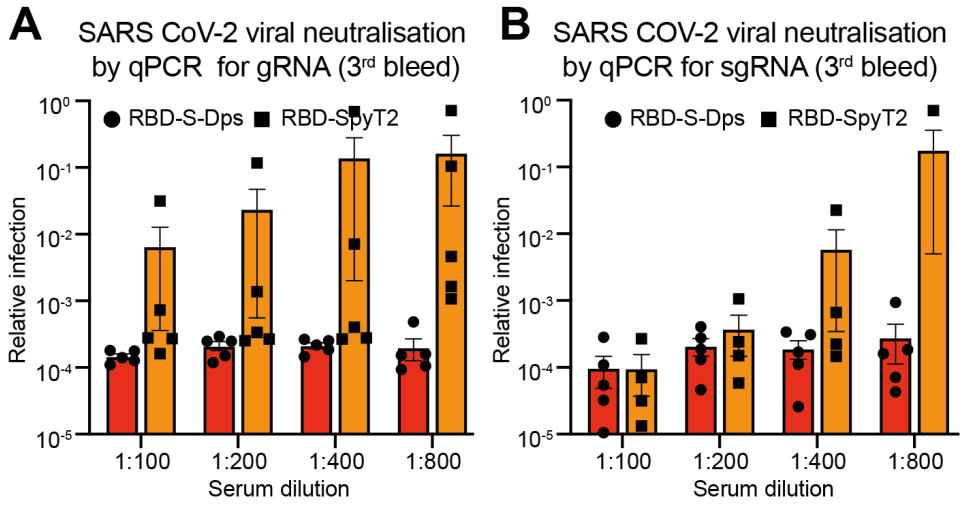

877

878 **A, B):** Vero cells expressing ACE2 and TMPRSS2 were infected with SARS-CoV-2 in the presence
879 of serial dilutions of antisera. Viral replication was then determined after 24 h by RT-qPCR using
880 probes for gRNA **(A)** or sgRNA **(B)**. Each point represents sera from an individual mouse.

881 **Supplemental Figure 3**

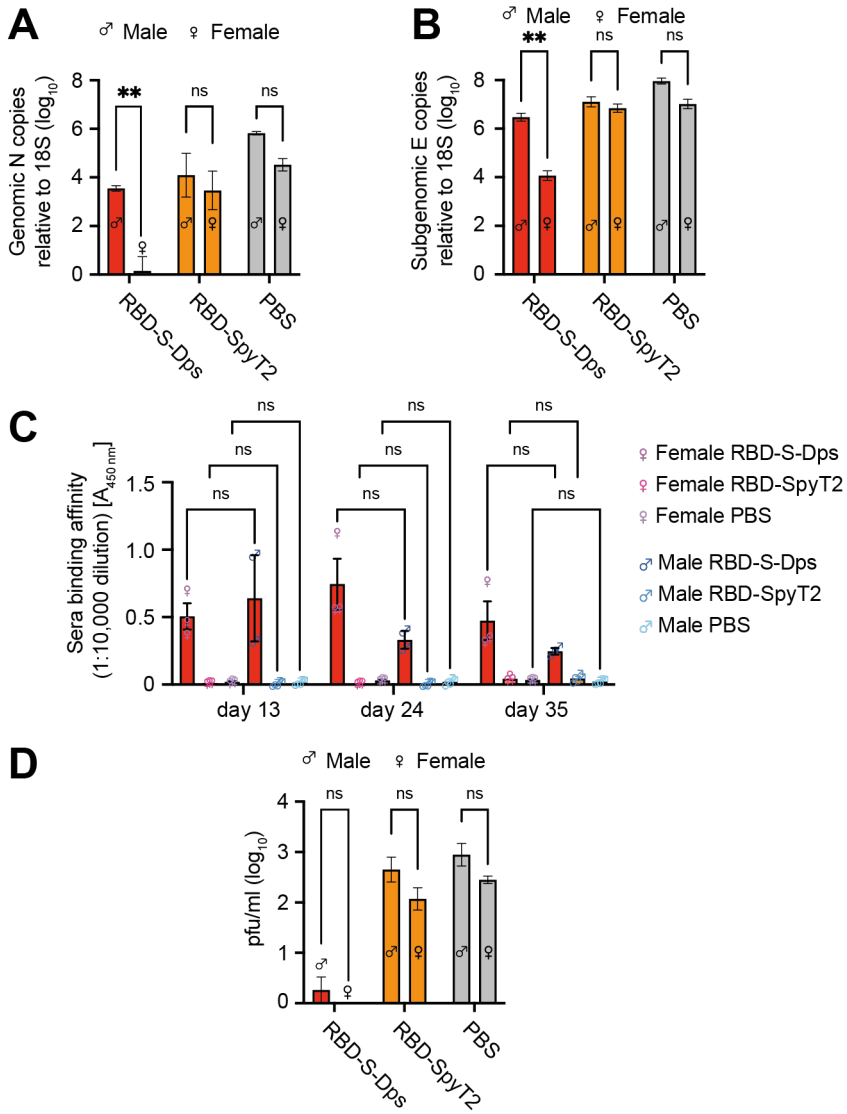

882

883 Mice were immunised with RBD-S-Dps, RBD-SpyT2 or given PBS control on day 1 and then
884 challenged with SARS-CoV-2 on day 28. **A & B)** Genomic and subgenomic (gRNA, sgRNA) qPCR
885 on RNA extracted from lung homogenates, using probes against NP or E, respectively. **C)** Sera
886 from days 13, 24 and 35 were tested for anti-RBD antibodies by ELISA. Two-way ANOVA tests
887 show that there are non-significant differences between male and female antibody responses.
888 **D)** Plaque assay using lung homogenates from mice culled seven days post-infection.

889 **Supplemental Figure 4**

890 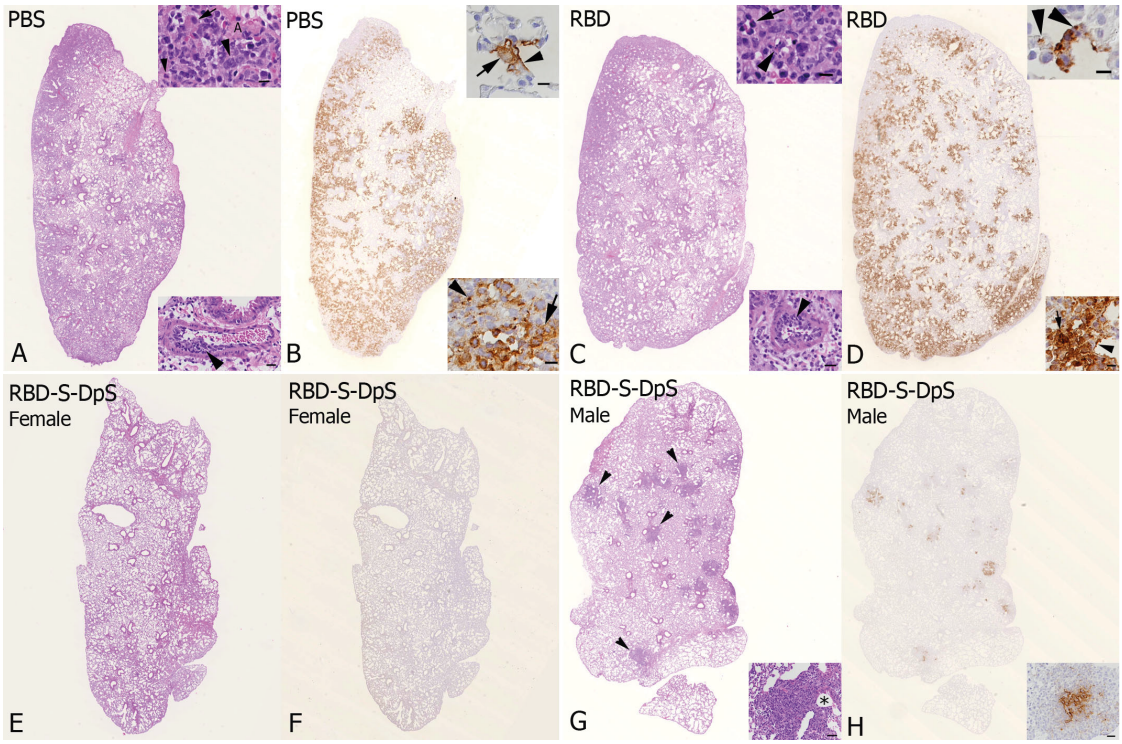

891 Lung, left lobe, K18-hACE2 mice at day seven post infection, SARS-CoV-2 challenge experiment.
892 Histological changes and SARS-CoV-2 antigen expression. **A, B: mice injected with PBS control.**
893 **A)** Overview of the lung lobe, with multifocal extensive cell-rich consolidated areas. Inset top:
894 consolidated area with activated type II pneumocyte (small arrow), syncytial cells (large
895 arrowhead) and infiltrating neutrophil (small arrowhead); A – alveolus (bar = 10 µm). Inset
896 bottom: artery with leukocyte infiltration of the wall (arrowhead; arteritis, bar = 20 µm). HE
897 stain. **B)** Extensive SARS-CoV-2 antigen expression is seen in multifocal patchy areas within and
898 close to consolidated areas, in pneumocytes and occasional macrophages. Inset top: alveolus
899 with viral antigen expression in type I (arrowhead) and type II (arrow) pneumocyte. Inset
900 bottom: consolidated area with viral antigen expression in macrophages (arrow) and
901 degenerate cells (arrowhead). Immunohistology, haematoxylin counterstain, bars = 10 µm. **C,**
902 **D: Monomeric RBD-SpyT2-immunised mice. C)** Overview of the lung lobe, with multifocal
903 extensive cell-rich consolidated areas. Inset top: consolidated area with several neutrophils
904 (arrowhead) and occasional necrotic cells (arrowhead, bar = 10 µm). Inset bottom: artery with
905 leukocyte infiltration of the wall (arrowhead; arteritis) and mild periarterial edema (bar = 20
906 µm). HE stain. **D)** Extensive SARS-CoV-2 antigen expression in multifocal patchy areas within

907 and close to consolidated areas, in pneumocytes and occasional macrophages. Inset top:
908 alveolus with viral antigen expression in pneumocytes of which some are degenerate
909 (arrowheads). Inset bottom: consolidated area with viral antigen expression in macrophages
910 (arrow) and type I pneumocyte (arrowhead). Immunohistology, haematoxylin counterstain;
911 bars = 10 µm. **E-H: Multimerised RBD-S-Dps immunised mice**. **E, F.** Female animal. **E)** Overview
912 of the lung lobe. The histological changes are restricted to focal areas of mildly increased
913 interstitial cellularity. HE stain. **F**) There is no evidence of viral antigen expression.
914 Immunohistology, haematoxylin counterstain. **G, H.** Male animal. **G)** Overview of the lung lobe,
915 with several small, randomly distributed peribronchiolar cell-rich areas (arrowheads). Inset:
916 Closer view of focal cell rich area (asterisk: bronchiole); bar = 50 µm, HE stain. **H**) SARS-CoV-2
917 antigen expression is restricted to the cell rich focal areas, in pneumocytes and occasional
918 macrophages (inset). Immunohistology, haematoxylin counterstain; bar = 20 µm.

919 **Supplemental Figure 5**

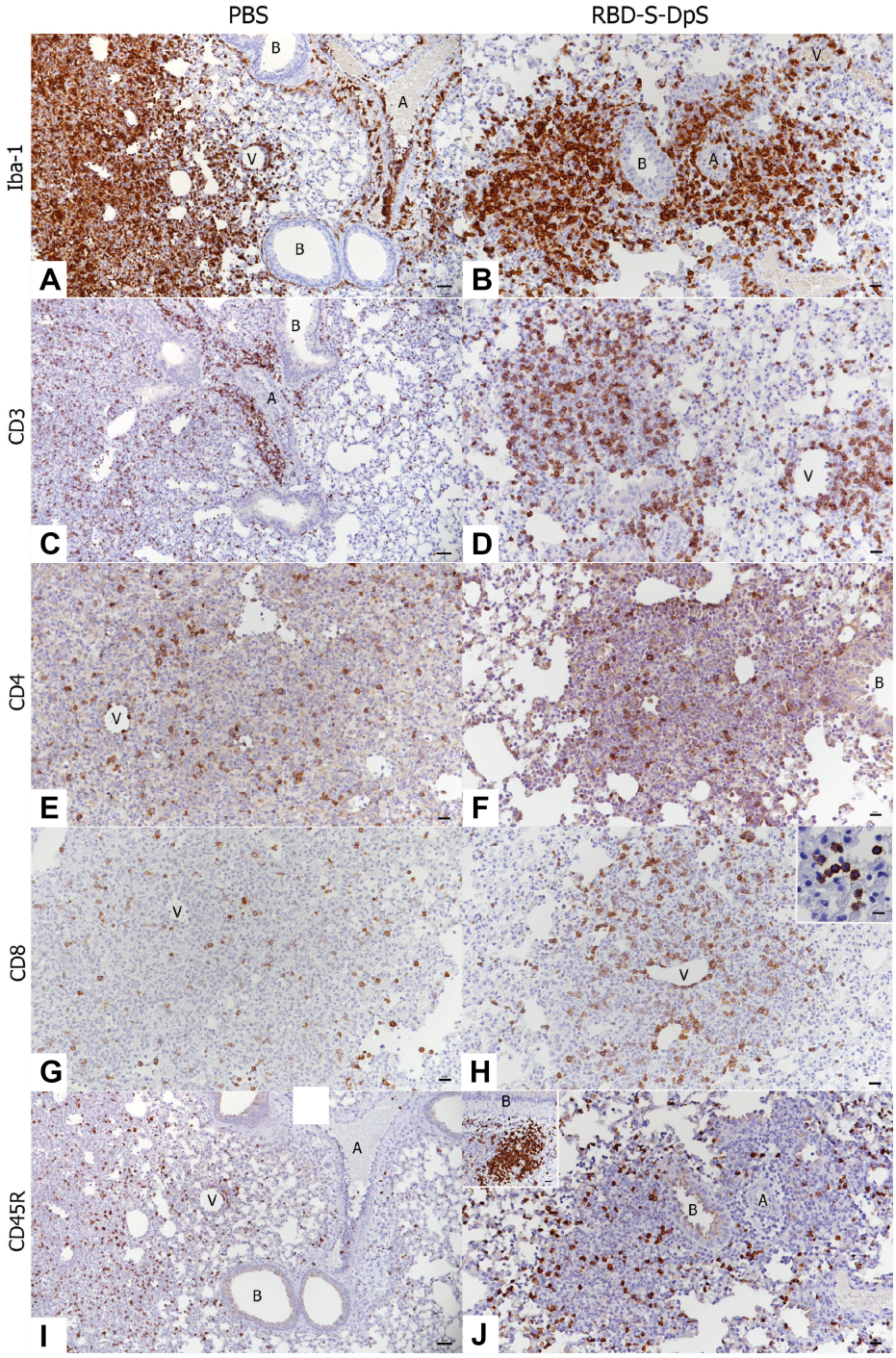

920

921 Lung, K18-hACE2 mice. Composition of the inflammatory infiltrates. **A, B:** staining for
922 macrophages (Iba1+). **A)** PBS-control animal. Macrophages are the dominant infiltrating cells
923 in the consolidated areas and in the vasculitis. A – artery with infiltration of the wall. V – vein

924 with infiltration of the wall. B – bronchiole. Bar = 50 µm. **B)** RBD-S-Dps animal, male.
925 Macrophages are the dominant infiltrating cells in the focal infiltrates. A – artery. V – vein. B –
926 bronchiole. Bar = 20 µm. **C, D:** staining for T cells (CD3+). **C)** PBS-control animal. T cells are
927 numerous in the consolidated areas and in the vasculitis. A – artery with infiltration of the wall
928 and perivascular T cell accumulation. B – bronchiole. Bar = 50 µm. **D)** RBD-S-Dps animal, male.
929 T cells are numerous in the focal infiltrates. V – vein. Bar = 20 µm. **E, F:** staining for CD4. **E)** PBS-
930 control animal. Within the infiltrates, CD4 positive cells are numerous. V – vein. Bar = 20 µm.
931 **F)** RBD-S-Dps animal, male. Within the infiltrates, CD4 positive cells are present in moderate
932 number. B – bronchiole. Bar = 20 µm. **G, H:** staining for CD8. **G)** PBS-control animal. CD8
933 positive cells are less numerous. V – vein. Bar = 20 µm. **H)** RBD-S-Dps animal, male. CD8 positive
934 cells are more abundant. V – vein. Bar = 20 µm. Inset: CD8 positive cells are also present in the
935 lumen of several alveoli. Bar = 10 µm. **I, J:** staining for B cells (CD45R/B220+). **I)** PBS-control
936 animal. B cells are observed in moderate numbers in the consolidated areas and are rare in the
937 vasculitis. A – artery with infiltration of the wall. V – vein with infiltration of the wall. B –
938 bronchiole. Bar = 50 µm. **J)** RBD-S-Dps animal, male. B cells (CD45R/B220+) are observed in
939 moderate numbers in the focal infiltrates. A – artery. B – bronchiole. Bar = 20 µm. Inset: Focal
940 peribronchial (B) B cell aggregate. Bar = 20 µm. Immunohistology, haematoxylin counterstain.

941 **Supplemental Table 1**

942 Amino acid sequences of the proteins used in this work. Signal sequences for secretion in
943 mammalian cells are indicated in red.

Protein	Amino acid sequence
SpyC2-Dps	MGHHHHHHGGSDSATHIKFSKRDEDGKELAGATMELRDSSGKTISTWISDGQVKDFYL YPGKYTFVETAAPDGYEVATAITFTVNEQGQVTVNGKATKGDAHIGSEGSSGGQDKPK EEPKVVGVEVLEKSGLDVKKLIEKLVKATAAEFTTYYYYTILRMHLTGMEGEGLKEIA EDARLEDRLHFELMTQRIYELGGNLPRDIRQLADLSACADAYLPENWKDPKEILKVLL EAEQCAIRTWKEVCDMTYGKDPRTYDLAQRILQEEIEHEAWFLELLYGRPSGHFRRSY PGEGPFSRKSRYE
SpyT2-NP (Nucleocapsid Protein)	MAHHHHHHGGSVPTIVMVDAYKRYKGGSGGSGGNTASWFTALTQHGKEDLKFPRGQGV PINTNSSPDDQIGYYRRATRRIRGGDGKMKDLSPRWYFYYLGTGPEAGLPYGANKDGI IWVATEGALNTPKDHIGTRNPANNAAIVLQLPQGTTLPKGFYAEGSRGGSQASSRSSS RSRNSSRNSTPGSSRGTSPARMAGNGGDAALALLLLDRLNQLESKMSGKGQQQQGQTV TKKSAAEASKKPRQKRTATKAYNVTQAFGRRGPEQTQGNFGDQELIRQGTDYKHWPQI AQFAPSASAFFGMSRIGMEVTPSGTWLTYTGAIKLDDKDPNFKDQVILLNKHIDAYKT FP
RBD-SpyT2	(MGILPSPGMPALLSLVSLLSVLLMGCVA) ETGITNLCPFGEVFNATRFASVYAWNRKRISNCVADYSVLYNSASFSTFKCYGVSPTK LNDLCFTNVYADSFVIRGDEVRQIAPGQTGKIADYNYKLPDDFTGCVIAWNSNNLDSK VGGNYNYLYRLFRKSNLKPFERDISTEIYQAGSTPCNGVEGFNCYFPLQSYGFQPTNG VGYQPYRVVVLSFELLHAPATVCGPKKGTGGSGGSGLNDIFEAQKIEWHEGGSHHHHH HHHGGSGGSGGSVPTIVMVDAYKRYK
Spike	(MGILPSPGMPALLSLVSLLSVLLMGCVA) ETGVNLTTRTQLPPAYTNSFTRGVYYPDKVFRSSVLHSTQDLFLPFFSNVTWFHAIHV SGTNGTKRFDNPVLPFNDGVYFASTEKSNIIRGWIFGTTLDSKTQSLLIVNNATNVVI KVCEFQFCNDPFLGVYYHKNNKSWMESEFRVYSSANNCTFEYVSQPFLMDLEGKQGNF KNLREFVFKNIDGYFKIYSKHTPINLVRDLPQGFSALEPLVDLPIGINITRFQTLLAL HRSYLTPGDSSSGWTAGAAAYYVGYLQPRTFLLKYNENGTITDAVDCALDPLSETKCT LKSFTVEKGIYQTSNFRVQPTESIVRFPNITNLCPFGEVFNATRFASVYAWNRKRISN CVADYSVLYNSASFSTFKCYGVSPTKLNDLCFTNVYADSFVIRGDEVRQIAPGQTGKI ADYNYKLPDDFTGCVIAWNSNNLDSKVGGNYNYLYRLFRKSNLKPFERDISTEIYQAG STPCNGVEGFNCYFPLQSYGFQPTNGVGYQPYRVVVLSFELLHAPATVCGPKKSTNLV KNKCVNFNFNGLTGTGVLTESNKKFLPFQQFGRDIADTTDAVRDPQTLEILDITPCSF GGVSVITPGTNTSNQVAVLYQDVNCTEVPVAIHADQLTPTWRVYSTGSNVFQTRAGCL IGAEHVNNSYECDIPIGAGICASYQTQTNSPGSASSVASQSIIAYTMSLGAENSVAYS NNSIAIPTNFTISVTTEILPVSMTKTSVDCTMYICGDSTECSNLLLQYGSFCTQLNRA LTGIAVEQDKNTQEVFAQVKQIYKTPPIKDFGGFNFSQILPDPSKPSKRSFIEDLLFN KVTLADAGFIKQYGDCLGDIAARDLICAQKFNGLTVLPPLLTDEMIAQYTSALLAGTI TSGWTFGAGAALQIPFAMQMAYRFNGIGVTQNVLYENQKLIANQFNSAIGKIQDSLSS TASALGKLQDVVNQNAQALNTLVKQLSSNFGAISSVLNDILSRLDPPEAEVQIDRLIT GRLQSLQTYVTQQLIRAAEIRASANLAATKMSECVLGQSKRVDFCGKGYHLMSFPQSA PHGVVFLHVTYVPAQEKNFTTAPAICHDGKAHFPREGVFVSNGTHWFVTQRNFYEPQI ITTDNTFVSGNCDVVIGIVNNTVYDPLQPELDSFKEELDKYFKNHTSPDVDLGDISGI NASVVNIQKEIDRLNEVAKNLNESLIDLQELGKYEQGSGYIPEAPRDGQAYVRKDGEW VLLSTFLGRSGGSLEVLFQGPGGSGLNDIFEAQKIEWHEGGSHHHHHH
Spike-SpyT2	(MGILPSPGMPALLSLVSLLSVLLMGCVA) ETGVNLTTRTQLPPAYTNSFTRGVYYPDKVFRSSVLHSTQDLFLPFFSNVTWFHAIHV SGTNGTKRFDNPVLPFNDGVYFASTEKSNIIRGWIFGTTLDSKTQSLLIVNNATNVVI KVCEFQFCNDPFLGVYYHKNNKSWMESEFRVYSSANNCTFEYVSQPFLMDLEGKQGNF

	KNLREFVFKNIDGYFKIYSKHTPINLVRDLPQGFSALEPLVDLPIGINITRFQTLLAL HRSYLTPGDSSSGWTAGAAAYYVGYLQPRTFLLKYNENGTITDAVDCALDPLSETKCT LKSFTVEKGIYQTSNFRVQPTESIVRFPNITNLCPFGEVFNATRFASVYAWNRKRISN CVADYSVLYNSASFSTFKCYGVSPTKLNDLCFTNVYADSFVIRGDEVRQIAPGQTGKI ADYNYKLPDDFTGCVIAWNSNNLDSKVGGNYNYLYRLFRKSNLKPFERDISTEIYQAG STPCNGVEGFNCYFPLQSYGFQPTNGVGYQPYRVVVLSFELLHAPATVCGPKKSTNLV KNKCVNFNFNGLTGTGVLTESNKKFLPFQQFGRDIADTTDAVRDPQTLEILDITPCSF GGVSVITPGTNTSNQVAVLYQDVNCTEVPVAIHADQLTPTWRVYSTGSNVFQTRAGCL IGAEHVNNSYECDIPIGAGICASYQTQTNSPGSASSVASQSIIAYTMSLGAENSVAYS NNSIAIPTNFTISVTTEILPVSMTKTSVDCTMYICGDSTECSNLLLQYGSFCTQLNRA LTGIAVEQDKNTQEVFAQVKQIYKTPPIKDFGGFNFSQILPDPSKPSKRSFIEDLLFN KVTLADAGFIKQYGDCLGDIAARDLICAQKFNGLTVLPPLLTDEMIAQYTSALLAGTI TSGWTFGAGAALQIPFAMQMAYRFNGIGVTQNVLYENQKLIANQFNSAIGKIQDSLSS TASALGKLQDVVNQNAQALNTLVKQLSSNFGAISSVLNDILSRLDPPEAEVQIDRLIT GRLQSLQTYVTQQLIRAAEIRASANLAATKMSECVLGQSKRVDFCGKGYHLMSFPQSA PHGVVFLHVTYVPAQEKNFTTAPAICHDGKAHFPREGVFVSNGTHWFVTQRNFYEPQI ITTDNTFVSGNCDVVIGIVNNTVYDPLQPELDSFKEELDKYFKNHTSPDVDLGDISGI NASVVNIQKEIDRLNEVAKNLNESLIDLQELGKYEQGSGYIPEAPRDGQAYVRKDGEW VLLSTFLGRSGTGGSGGSGLNDIFEAQKIEWHEGGSHHHHHHHHGGSGGSGGSVPTIV MVDAYKRYK

944